Accepted manuscript. Published in International Journal of Solids and Structures (2021). Version of record: https://doi.org/10.1016/j.ijsolstr.2021.111041.
© 2021. This manuscript version is made available under the CC-BY-NC-ND 4.0 license https://creativecommons.org/licenses/by-nc-nd/4.0/

Mechanics of shrinkage-swelling transition of microporous materials at the initial stage of adsorption

Mehdi Eskandari-Ghadi[1] and Yida Zhang[2*]

ABSTRACT

This work extends the recently developed surface poromechanics theory to explain the unusual contraction behaviour of some microporous materials at the early stage of adsorption. In micropores, the overlap of adsorbed layers near opposing solid walls can give rise to forces that are formerly disregarded in the analysis of macro/meso porous materials. The effect of these interactions is studied at the microscale with reference to a slit pore geometry through pore-scale thermodynamic analysis. As a result, an extra pressure normal to the pore walls known as the disjoining pressure, in addition to the bulk fluid pressure that is typically considered for macro/meso pores, is obtained for micropores. This term also modifies the surface tension parallel to the pore walls. The disjoining pressure and the modified surface tension together create a competing effect depending on which, the material can exhibit shrinkage or swelling during adsorption at low gas pressures, which has been experimentally observed in various microporous solids since the 1950s. By adopting proper adsorption and microstructure models with physically meaningful parameters, the theory is validated against the recent adsorption-deformation data of microporous carbon interacting with nitrogen, argon, and carbon dioxide gases. For the first time, the abnormal contraction of porous materials upon initial gas uptake is quantitatively modelled through poromechanics that considers surface forces developed in micropores. The proposed theory offers a rigorous procedure to upscale the disjoining pressure and surface tension operating at pore-scale to the adsorption stresses felt by the overall solid skeleton, effectively preserving the characteristics of solid-adsorbate interaction in the continuum modelling of microporous materials.

KEYWORDS

Poromechanics, Microporous solids, Adsorption, Swelling/ shrinkage, Interface

[1] Graduate student, University of Colorado Boulder, Boulder, CO, USA.
[2] Assistant professor, University of Colorado Boulder, Boulder, CO, USA. Email: yida.zhang@colorado.edu

1 INTRODUCTION

Materials with pore size smaller than 2 nm in diameter are *microporous* per IUPAC classification (Everett, 1972). A common property of microporous materials is that substantial swelling/shrinkage can be induced by adsorption/desorption of fluid molecules, which plays important roles in various engineering applications and natural processes. Reversible adsorption-deformation processes can serve as fast and reliable actuation mechanisms in making gas sensors and actuators (Zhao et al., 2014). Pine cones open and close scales upon changes of air humidity to release their seeds (Bertinetti et al., 2013; Van Opdenbosch et al., 2016). Undesired sorption strain can also adversely impact the serviceability of these materials by causing cracking (Colina and Roux, 2000), degradation (Baek and Pence, 2009), plastic deformation (Hansen, 1987) and even structural transitions (Serre et al., 2002). There is therefore an immediate need to deepen our understanding and develop predictive theories for adsorption-deformation coupling in porous materials. In particular, Gor et al. (2017) summarized two key questions such a theory needs to answer: **Q1**) How to predict the stresses in the pores induced by the fluid adsorption? and **Q2**) how do these stresses affect a porous material, so that the resulting strains are observed?

One of the earliest rationalizations of adsorption-deformation coupling is by Bangham and his co-workers (Bangham and Fakhoury, 1928; Bangham and Razouk, 1938). They attributed such swelling to the reduced surface energy due to adsorption, which relaxes the solid-fluid interface and causes expansion of the porous skeleton. Such effect is now referred to as the *Bangham effect*. Early empirical models adopt Langmuir-like equations to directly link the swelling strain to gas pressure (Chikatamarla et al., 2004; Levine, 1996; Palmer and Mansoori, 1996). A more rigorous treatment is given by Coussy (2010) and Vandamme et al. (2010) who have modified the standard free energy balance of saturated porous solid and derived the stresses conjugated to the swelling strain:

$$\sigma_a = \gamma \frac{\partial A_s}{\partial \varepsilon}; p_a = \gamma \frac{\partial A_s}{\partial \phi} \tag{1}$$

where γ is surface energy which should be replaced by surface stress if surface deformation is significant (Shuttleworth, 1950); A_s the volume-specific surface area; ε and ϕ the volumetric strain and porosity, respectively; σ_a and p_a are the so-called *adsorption stresses* that collectively represent the additional stresses felt by an adsorptive porous skeleton compared to its inert or non-adsorptive

counterpart. Eq. (1) shows that the adsorption stresses are not only functions of surface energy but also dependent on the morphology of the pore network reflected through the function $A_s(\varepsilon,\phi)$. Quantitative predictions of swelling strain can be made by combining Eq. (1) with standard poroelastic models (Espinoza et al., 2013). Recently, instead of assuming a free energy expression, Zhang (2018) studied the fundamental balance laws of saturated surface-active porous media by treating the solid-fluid interface as an independent phase (which is referred to as *surface poromechanics* hereafter for simplicity) and arrived at the same adsorption stress expression in Eq. (1). This confirmed that adsorption stresses are not constitutive hypotheses but are natural results of energy conservation in sorptive porous systems.

The Bangham effect alone, however, cannot explain the full spectrum of adsorption-deformation phenomena observed in microporous materials. Experimental studies on activated carbons, porous glasses, zeolites, and porous silicon found that contraction takes place first at low gas pressure, followed by Bangham's expansion after reaching certain pressure levels (Amberg and McIntosh, 1952; Dolino et al., 1996; Gor et al., 2017; Haines and McIntosh, 1947; Lakhanpal and Flood, 1957). No consensus has arrived regarding the mechanisms responsible for such initial contraction. Lakhanpal and Flood (1957) suggested that the presence of opposite walls in micropores may form a "bridge" made of adsorbate molecules, which can induce some sorts of contraction forces and shrink the pores. From a thermodynamic viewpoint, Ash et al. (1973) showed that a pressure called the *disjoining pressure* normal to the pore wall arises when reducing the pore size to nanometre scale. This creates two levels of competition: First, the disjoining pressure could be repulsive or attractive as the pore size is reduced, depending on the competition between the increased attractive potential and the decreased pore space to host adsorbate molecules (Gor et al., 2017). Second, even if the disjoining pressure is attractive, it must compete against the relaxation of surface tension to create shrinkage effect (Dolino et al., 1996).

Quantitative comparison of these forces in the context of varying gas pressure and pore sizes has never been done to the authors' knowledge. Moreover, none of these pore-scale mechanisms have been integrated into the continuum descriptions of microporous solids. Brochard et al. (2012) presented a generic theory for microporous media where they have removed the notion of porosity and specific surface area, arguing that these quantities cannot be unambiguously defined. Such treatment is almost too general that the derived constitutive relation is essentially a linear chemoelasticity model that disconnects with pore-scale mechanics. In fact, Anand (2015) showed that linear poroelasticity is a

special case of chemoelasticity after supplying some microstructural information such as porosity. Pijaudier-Cabot and his co-workers (Pijaudier-Cabot et al., 2011; Vermorel and Pijaudier-Cabot, 2014) have introduced the concepts of equivalent porosity or equivalent pore pressure in Coussy's framework to account for the interaction forces in micropores. However, they acknowledged that the theories cannot reproduce the early shrinkage effect. Another approach to this problem is based on molecular-scale analysis. Ravikovitch and Neimark (2006) provided a direct evaluation of adsorption stress based on intermolecular forces using the nonlocal density functional theory (NLDFT), thus offering a physically sound answer to the first question Q1. Such computation is, however, too expensive to be integrated into continuum models that deals with the smeared behaviour of porous materials that contain millions of pores. Because of this, their calculation of adsorption strain is based on an oversimplified mechanical model that assumes incompressible, isotropic, and linear solid phase without considering shear stresses. Thus, a satisfactory answer to the second question Q2 is still lacking.

The purpose of this study is therefore to develop a continuum theory that marries the physical soundness of microscale approaches in calculating adsorption stresses and the generality of continuum poromechanics in modelling adsorption induced shrinkage-swelling strains of microporous solids. To achieve this, the framework of surface poromechanics is laid out in Section 2. Pore-scale thermodynamic analysis that reveals the surface forces generated by adsorption is performed in Section 3. These forces are then upscaled and integrated into the continuum description of deformable porous media in Section 4. Section 5 examines the performance of the theory in capturing the adsorption-deformation behaviour of microporous carbon interacting with CO_2, N_2 and Ar gases especially at low gas pressures. Finally, the main conclusions and possible future directions of this work are discussed in Section 6.

2 SURFACE POROMECHANICS

Classical poromechanics describes the hydromechanical behaviour of a non-adsorptive porous skeleton (solid) filled by inert pore fluid (liquid or gas). If the physiochemical interactions between the two phases are sufficiently strong, an increase of fluid concentration in the vicinity of the solid-fluid interface (or simply *adsorption*) may be observed (Fig. 1). The properties of the fluid in the adsorbed layers differ from those of the bulk fluid, and thus the classical two-phase conceptualization breaks down. A way to simplify the picture is via Gibbs' excess convention (DeHoff, 2006), where a hypothetical zero-thickness surface phase is defined in the interfacial zone to lump the properties of the

adsorbed layers. Based on such convention, surface poromechanics (Zhang, 2018) treats adsorptive porous materials as a three-phase media including the solid, the bulk fluid, and the surface phases, each possesses independent thermodynamic and kinematic properties. As a result, surface tension which is a function of solid-fluid interaction naturally appears in the macroscopic Ψ-potential of the solid skeleton, permitting a mechanistic modelling of adsorption-induced swelling of meso/macroporous materials. The interest here is to generalize such approach to describe microporous materials where the unusual behaviour of adsorption-shrinkage at low pressures is observed.

The system of interest is depicted in Fig. 1. The main difference here compared to Zhang (2018) is that the adsorbed layers of two opposing solid walls now may interact, representing the case of microporous materials (see Section 3.1 for more discussions). The motion of the solid is described by $\mathbf{x}=\mathbf{x}(\mathbf{X},t)$, where $\mathbf{x}$ is the current spatial position of the solid particle at time t, and $\mathbf{X}$ is the position of the solid particle at time $t=0$. A line segment $d\mathbf{X}$ and a volume element $d\Omega_0$ in the reference configuration are respectively mapped to the current configuration $d\mathbf{x}$ and $d\Omega_t$ via $d\mathbf{x}=\mathbf{F}\cdot d\mathbf{X}$ and $d\Omega_t = Jd\Omega_0$, where $\mathbf{F}=\nabla_X\mathbf{x}$ is the deformation gradient and $J=\det\mathbf{F}$ is the Jacobian. By defining the displacement vector $\mathbf{u}^s=\mathbf{x}-\mathbf{X}$, the Green-Lagrange strain is written as $\mathbf{E}=(\nabla_X\mathbf{u}^s+{}^T\nabla_X\mathbf{u}^s+{}^T\nabla_X\mathbf{u}^s\cdot\nabla_X\mathbf{u}^s)/2$. ∇_X denotes gradient with respect to material coordinate $\mathbf{X}$. The Eulerian description of the solid kinematics involves the rate of deformation $\mathbf{D}=(\nabla_x\mathbf{v}^s+{}^T\nabla_x\mathbf{v}^s)/2$ where $\mathbf{v}^s(\mathbf{x},t)$ is the velocity vector of the particle originally at $\mathbf{X}$ in the reference configuration and passing through point $\mathbf{x}$ at time t, while ∇_x denotes gradient with respect to spatial coordinate $\mathbf{x}$. $\mathbf{D}$ can be expressed in terms of $\mathbf{E}$ through $\mathbf{D}={}^T\mathbf{F}^{-1}\cdot(d\mathbf{E}/dt)\cdot\mathbf{F}^{-1}$. Ω_t^v denotes the void space occupied by the bulk fluid in the representative current volume Ω_t. For conciseness, we drop the subscript t in Ω_t and Ω_t^v hereafter. The Eulerian and Lagrangian porosities, n and ϕ, are defined by $\Omega^v=n\Omega=\phi\Omega_0$. The Eulerian and Lagrangian specific surface areas, a_s and A_s, are introduced to denoted the amount of interface $\mathcal{A}$ per unit current and reference volume $\mathcal{A}=a_s\Omega=A_s\Omega_0$, respectively. The velocity and density of phase α $(=s,f,\text{or}\,surf)$ are denoted by $\mathbf{v}^\alpha$ and ρ^α, respectively, where s, f, and $surf$ respectively correspond to the solid, the fluid, and the surface phases. Naturally, all intensive quantities of the solid and the fluid phases are expressed as per unit

volume, while the same quantities are expressed as per unit area for the surface phase. The particle derivative of a field with respect to phase α is defined as (Coussy, 2004):

$$\frac{d^{\alpha}}{dt}(\cdot)=\frac{\partial}{\partial t}(\cdot)+\mathbf{v}^{a}\cdot\nabla_{x}(\cdot) \tag{2}$$

It is assumed here that the surface moves together with the solid skeleton as illustrated in Fig. 1 (i.e. $\mathbf{v}^{surf}=\mathbf{v}^{s}$). Thus $d^{s}(\cdot)/dt$ and $d^{surf}(\cdot)/dt$ are identical and only the former will be used for conciseness. In the following, upper- and lower-case Greek letters denote quantities in reference and current configurations, respectively. Letters with hat denote mass-specific quantities (e.g. mass-specific fluid internal energy $\hat{e}^{f}$).

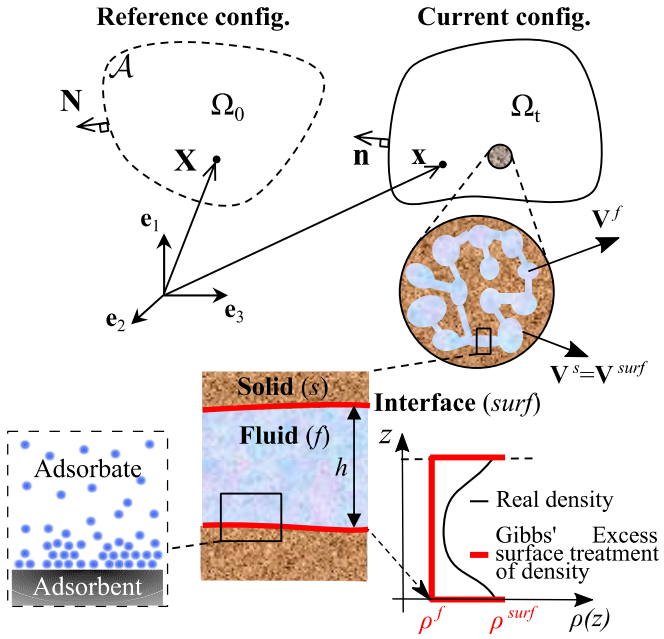

Fig. 1. A schematic of an adsorptive microporous material and Gibbs' excess treatment of the adsorbed layer

The mass balance equations for the solid, the surface and the fluid phases with respect to a fixed observing window on the solid phase can be written as

$$\frac{d^{s}\rho^{s}(1-n)}{dt}+\rho^{s}(1-n)\nabla_{x}\cdot\mathbf{v}^{s}=0 \tag{3}$$

$$\frac{d^{s}\rho^{surf}a^{s}}{dt}+\rho^{surf}a^{s}\nabla_{x}\cdot\mathbf{v}^{s}-\hat{r}=0 \tag{4}$$

$$\frac{d^s(\rho^f n)}{dt} + \rho^f n \nabla_x \cdot \mathbf{v}^s + \nabla_x \cdot \hat{\mathbf{w}} + \hat{r} = 0 \tag{5}$$

where $\hat{\mathbf{w}} = \rho^f n(\mathbf{v}^f - \mathbf{v}^s)$ is the fluid flow vector relative to the solid motion; $\hat{r}$ is the rate of mass exchange between the surface and the fluid phases due to adsorption/desorption. The total traction vector $\mathbf{T}$ acting upon the boundary of Ω_t can be decomposed into the partial traction vectors $\mathbf{T}^\alpha$ acting on the boundary of phase α such that $\mathbf{T} = \sum_\alpha \mathbf{T}^\alpha$. Thus, one may define the total stress tensor $\boldsymbol{\sigma}$ and partial stress tensor $\boldsymbol{\sigma}^\alpha$ respectively as $\mathbf{T} = \boldsymbol{\sigma} \cdot \mathbf{n}$ and $\mathbf{T}^\alpha = \boldsymbol{\sigma}^\alpha \cdot \mathbf{n}$ with $\boldsymbol{\sigma} = \sum_\alpha \boldsymbol{\sigma}^\alpha$. The balance of linear momentum can thus be written for individual phases (Zhang, 2018) and summed with use of Eqs. (3)-(5) to obtained that of the entire system:

$$\nabla_x \cdot \boldsymbol{\sigma} + \left[\rho^s(1-n) + \rho^{surf} a_s\right]\left[\mathbf{f} - \mathbf{a}^s\right] + \rho^f n\left[\mathbf{f} - \mathbf{a}^f\right] = \mathbf{0} \tag{6}$$

where $\mathbf{a}^\alpha = d^\alpha \mathbf{v}^\alpha / dt$ is the acceleration vector of phase α. Similarly, the energy balance (or the first law of thermodynamics) can be written for each phase (Zhang, 2018) and summed to obtain the overall energy balance as

$$\frac{d^s e}{dt} + e\nabla_x \cdot \mathbf{v}^s = \boldsymbol{\sigma} : \mathbf{D} - \nabla_x \cdot \left(\hat{h}^f \hat{\mathbf{w}}\right) + (\mathbf{f} - \mathbf{a}^f) \cdot \hat{\mathbf{w}} - \nabla_x \cdot \mathbf{q} \tag{7}$$

or

$$\frac{\partial E}{\partial t} = \mathbf{S} : \frac{\partial \mathbf{E}}{\partial t} - \nabla_X \cdot \left(\hat{h}^f \hat{\mathbf{W}}\right) + (\mathbf{f} - \mathbf{a}^f) \cdot \mathbf{F} \cdot \hat{\mathbf{W}} - \nabla_X \cdot \mathbf{Q} \tag{8}$$

where $e = \rho^s(1-n)\hat{e}^s + \rho^{surf} a_s \hat{e}^{surf} + \rho^f n \hat{e}^f$ and $E = \rho^s(J-\phi)\hat{E}^s + \rho^{surf} A_s \hat{E}^{surf} + \rho^f \phi \hat{E}^f$ are the total internal energies per unit current and reference volumes, respectively; $\mathbf{q}$ and $\mathbf{Q} = J\mathbf{F}^{-1} \cdot \mathbf{q}$ are respectively the Eulerian and Lagrangian surface heat flux vectors; $\hat{h}^f$ is the mass-specific enthalpy of the fluid; $\mathbf{S} = J\mathbf{F}^{-1} \cdot \boldsymbol{\sigma} \cdot \mathbf{F}^{-T}$ is the Second Piola-Kirchhoff stress tensor; and $\hat{\mathbf{W}} = J\mathbf{F}^{-1} \cdot \hat{\mathbf{w}}$ is the Lagrangian relative flow vector. The second law can be written for the entire system as

$$\frac{d^s s}{dt} + s\nabla_x \cdot \mathbf{v}^s \geq -\nabla_x \cdot \left(\hat{s}^s \hat{\mathbf{w}} + \frac{\mathbf{q}}{T}\right) \tag{9}$$

or

$$\frac{\partial S}{\partial t} \geq -\nabla_X \cdot \left(\hat{s}^s \hat{\mathbf{W}} + \frac{\mathbf{Q}}{T} \right) \tag{10}$$

where $s = \rho^s (1-n)\hat{s}^s + \rho^{surf} a_s \hat{s}^{surf} + \rho^f n \hat{s}^f$ and $S = \rho^s (J-\phi)\hat{S}^s + \rho^{surf} A_s \hat{S}^{surf} + \rho^f \phi \hat{S}^f$ are the entropy of the material per unit current and reference volumes, respectively. The Clausius-Duhem inequality is thus deduced by substituting Helmholtz free energy per unit reference volume, $\Psi = E - TS$, into Eq. (10) and introducing total dissipation rate Φ:

$$\Phi = \frac{\partial E}{\partial t} - S\frac{\partial T}{\partial t} + T\nabla_X \cdot \left(\hat{s}^s \hat{\mathbf{W}} + \frac{\mathbf{Q}}{T} \right) - \frac{\partial \Psi}{\partial t} \geq 0 \tag{11}$$

Substituting Eq. (8) into Eq. (11), the total dissipation can be decomposed into the material dissipation Φ_M, the mass transport dissipation Φ_H, and the thermal dissipation Φ_T (Zhang, 2018), each can be considered non-negative due to the relative independence of the processes causing these dissipations. The latter two embody the classical Darcy's and Fourier's laws, while the material dissipation serves as a thermodynamic constraint for the possible constitutive laws of the material representative elementary volume (REV):

$$\Phi_M = \mathbf{S} : \frac{\partial \mathbf{E}}{\partial t} + \hat{g}^f \frac{\partial \rho^f \phi}{\partial t} + \hat{\mu}^f M \frac{\partial \Gamma A_s}{\partial t} - S\frac{\partial T}{\partial t} - \frac{\partial \Psi}{\partial t} \geq 0 \tag{12}$$

where $\hat{g}^f$ and $\hat{\mu}^f$ are the mass-specific Gibbs' free energy and chemical potential of the fluid, respectively; M is the molar mass of the fluid species, and Γ is the number of moles of adsorbed fluid molecules per unit current area on the surface phase, or simply the surface excess concentration. Knowing the REV consists of three phases, the material dissipation can be further decomposed into three relatively independent contributions:

$$\Phi_M = \Phi_M^s + \Phi_M^{surf} + \Phi_M^f \geq 0 \tag{13}$$

where $\Phi_M^s, \Phi_M^{surf}, \Phi_M^f$ denote the solid, surface and fluid part of the material dissipation, respectively. Such decomposition seems arbitrary but is indeed guided by the principle that each free energy balance equation (i.e. $\Phi_M^s = 0, \Phi_M^{surf} = 0, \Phi_M^f = 0$) should embody the state equations of the corresponding phase derived independently from homogeneous systems. Zhang (2018) decomposed Eq. (12) to retrieve the

free energy expressions of the bulk fluid and the surface phases for meso/macro pores based on the assumption of free adsorption where the classical Gibbs isotherm applies. However, the overlapping of interfacial zones of opposite walls in micropores (as sketched in Fig. 1) requires a new energy partition to account for such interactions. To make sure the state equations of the fluid and surface phases in micropores can be correctly retrieved from Eq. (12), one must delve into the physics and thermodynamics of adsorption in an individual micropore.

3 PORE-SCALE ANALYSIS

3.1 SURFACE FORCES IN A SLIT PORE

Consider a slit pore that consists of two solid walls with their gap filled by the pore fluid as shown in Fig. 2. Near each surface, the fluid molecules are influenced by surface forces including van der Waals, electrostatic and hydration forces (Israelachvili, 2011), causing certain structural ordering of the fluid molecules parallel to the planar pore walls and forming an interfacial region in which the thermodynamic properties differ from both adjacent phases (DeHoff, 2006). As a consequence of such structuring, fluid pressure near the surface becomes anisotropic with the pressure component tangential

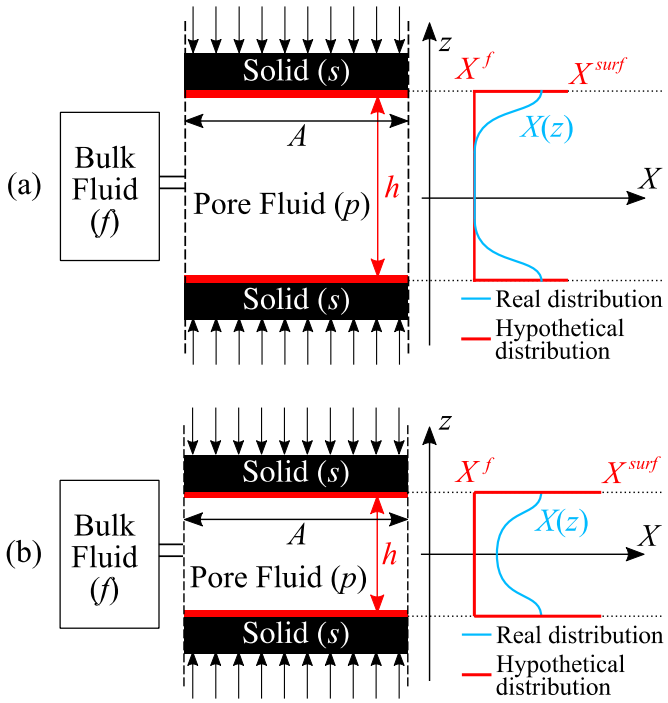

Fig. 2. Real versus hypothetical system (Gibbs' excess surface treatment) for studying thermodynamics of adsorption in a rigid slit pore: (a) meso/macro pores where the adsorbed regions do not overlap; (b) micropores in which the adsorbed regions overlap. X can be the fluid density or other intensive quantities like free energy or the tangential pressure of the pore fluid (but perhaps with a different profile)

to the wall varies with respect to the distance from the wall and the normal component the same everywhere (de Feijter, 1988; Sarman et al., 1987). The difference between the tangential and the normal pressures gives rise to the surface tension according to the Bakker's equation (Wien et al., 1928).

For *meso/macropores* which exclusively refer to relatively large pores with non-overlapping interfacial regions in this study (Fig. 2a), the fluid phase in the middle regime has the same properties as the bulk fluid in equilibrium with the pore fluid. The treatment of the pore surfaces therefore has no difference compared to that for a single solid surface subjected to free adsorption. The Helmholtz free energy and internal energy of the surface phase therefore can be directly written as (Zhang, 2018):

$$dF^{surf} = -S^{surf}dT + \gamma dA + \mu dN^{surf} \tag{14}$$

$$dU^{surf} = TdS^{surf} + \gamma dA + \mu dN^{surf} \tag{15}$$

where S^{α} and N^{α} represent the entropy and number of moles in phase α, respectively; T the temperature of the system; A the total surface area of the slit pore (twice of that of the upper/lower surface); and μ the chemical potential of the adsorbate. It is worth noting that, in writing Eqs. (14) and (15), we have omitted the work associated with stretching of the solid surface. For this reason, it is the surface energy that is conjugate to the change of surface area instead of the surface stress (Shuttleworth, 1950). This assumption may be relaxed in the future to capture the two-way coupling between adsorption and deformation as discussed in Zhang (2018). For a system consisting of λ copies of the same pore, the entropy, surface area, number of moles in the surface phase, and the surface internal energy must be λ times of those of a single pore: $U^{surf}(\lambda S^{surf}, \lambda A, \lambda N^{surf}) = \lambda U^{surf}(S^{surf}, A, N^{surf})$. Thus, according to Euler's homogenous function theorem, U^{surf} is a homogeneous function of degree one and can be written in total form as

$$U^{surf} = TS^{surf} + \gamma A + \mu N^{surf} \tag{16}$$

Subtracting the total derivative of Eq. (16) by Eq. (15) and considering isothermal condition gives the celebrated Gibbs isotherm:

$$d\gamma = -\Gamma d\mu \tag{17}$$

where $\Gamma \equiv N^{surf} / A$ is the surface excess concentration as appeared in Eq. (12). The total internal energy, entropy and molar content of the overall pore fluid can be written respectively as:

$$dU_p = dU^f + dU^{surf};\ dS_p = dS^f + dS^{surf};\ dN_p = dN^f + dN^{surf} \tag{18}$$

where the subscript p denotes properties belonging to the overall pore fluid which include the surface excess phase and the bulk fluid phase. Substituting the internal energy of the bulk fluid (DeHoff, 2006):

$$dU^f = TdS^f - pdV^f + \mu dN^f \tag{19}$$

and Eq. (15) into (18) gives the internal energy of the pore:

$$dU_p = TdS_p - pdV^f + \gamma dA + \mu dN_p \tag{20}$$

Since the pore fluid is in equilibrium with its surrounding solid phase, the physical implication of Eq. (20) is that the pore walls feel a normal pressure p (same as the bulk fluid pressure) that conjugates to the change of pore volume and a tangential stress γ which conjugates to the change of surface area. Classical poromechanics (Biot and Temple, 1972; Coussy, 2004) only considers p in modelling saturated porous media, while the extended theory (Zhang, 2018) has retrieved both p and γ in the macroscopic Ψ-potential that is useful in modelling Bangham's expansion upon fluid adsorption.

If the pore walls are brought sufficiently close together, the interfacial regions can overlap, creating an interaction force normal to the pore walls (Gor et al., 2017). All fluid molecules in this case become structurally ordered to some extent and nowhere in the pore resembles the bulk fluid properties (Fig. 2b). The term *micropore* in this study is reserved for pores that contain overlapped interfacial regions as opposed to meso/macro pores defined previously. Energetic wise, such interaction implies that an extra work dW is needed to bring the two surfaces together, in addition to the work required to overcome the bulk fluid pressure:

$$dW = \frac{1}{2} A dw = -\frac{1}{2} A \Pi dh \tag{21}$$

where h is the pore size; $dw \equiv -\Pi dh$ is the area-specific extra work; $A/2$ is the area of a single surface; Π is the thermodynamic pressure conjugated to the change of pore size, the physical meaning of which shall be revealed soon.

We again idealize the nanoconfined pore fluid in Fig. 2b as a superposition of a bulk fluid phase and a surface excess phase. This idea is inspired by literatures in thin-film physics, where the Gibbs excess convention has been versatilely used to describe thin liquid films (de Feijter, 1988; Rusanov, 1966). By

247 supplementing Eq. (21) in the energy balance of the pore system, the Helmholtz free energy of the
248 surface phase becomes:

249 $$dF^{surf} = -S^{surf}dT + \gamma dA + \mu dN^{surf} \overbrace{-\frac{1}{2}A\Pi dh}^{+dW} \tag{22}$$

250 with the energy equations of the bulk fluid phase remains the same as in Eq. (19). Indeed, Eq. (22) is
251 identical to the free energy balance of the interface of thin liquid films (de Feijter, 1988), which is
252 expected because of the similarity between the nanoconfined fluid in a slit pore and a liquid film
253 stretched to nanometre thickness. Comparing Eq. (22) with Eq. (14), we can see that the effect of
254 overlapped interfacial regime is solely reflected through an additional term dW in the free energy of the
255 surface phase. Therefore, the pressure Π can be considered as a property belonging to the surface phase
256 just like the surface energy γ. Eq. (22) gives the thermodynamic definition of γ and Π:

257 $$\gamma = \left.\frac{\partial F^{surf}}{\partial A}\right|_{T,h,N^{surf}} \text{ and } \Pi = -\frac{2}{A}\left.\frac{\partial F^{surf}}{\partial h}\right|_{T,A,N^{surf}} \tag{23}$$

258 Eq. (22) can be rewritten considering the volume of a slit pore $V^f = Ah/2$:

259 $$dF^{surf} = -S^{surf}dT - \Pi dV^f + \left(\gamma + \frac{1}{2}\Pi h\right)dA + \mu dN^{surf} \tag{24}$$

260 The corresponding internal energy is:

261 $$dU^{surf} = TdS^{surf} - \frac{1}{2}A\Pi dh + \gamma dA + \mu dN^{surf} \tag{25}$$

262 or equivalently:

263 $$dU^{surf} = TdS^{surf} - \Pi dV^f + \left(\gamma + \frac{1}{2}\Pi h\right)dA + \mu dN^{surf} \tag{26}$$

264 Substituting Eqs. (19) and (26) into Eq. (18) gives the total internal energy of the pore fluid:

265 $$dU_p = TdS_p - \overbrace{(p+\Pi)}^{p_p}dV^f + \overbrace{\left(\gamma + \frac{1}{2}\Pi h\right)}^{\gamma_p}dA + \mu dN_p \tag{27}$$

Comparing Eq. (27) with its counterpart for macro/mesopores Eq. (20), it is apparent that the equivalent pore pressure felt by its surrounding (i.e. the solid walls) is deviated from the bulk fluid pressure p by amount of Π:

$$p_p = p + \Pi \tag{28}$$

Eq. (28) reveals that Π physically corresponds to the pressure difference between the pore pressure locally acting on the pore walls and the bulk fluid pressure in a connected reservoir in equilibrium with the pore. It is termed as *disjoining pressure* after Derjaguin and Kusakov (1936) and sometimes referred to as *solvation pressure* (Gor et al., 2017; Vandamme, 2019). Π can be repulsive (positive) or attractive (negative) depending on the sign of dW. By similar comparison, the equivalent surface tension felt by the solid walls in a micropore is modified to:

$$\gamma_p = \gamma + \frac{1}{2}\Pi h \tag{29}$$

Since Π and γ_p arises from interactions between two closely spaced pore surfaces, we collectively refer to them as the *surface force* terms hereafter. A system consisting λ copies of the same micropore must have an internal energy of λU^{surf} and volume and surface area of λV^f and λA. Thus Eq. (26) is a homogeneous function of degree one

$$U^{surf}(\lambda S^{surf}, \lambda V^f, \lambda A, \lambda N^{surf}) = \lambda U^{surf}(S^{surf}, V^f, A, N^{surf}) \tag{30}$$

and therefore:

$$U^{surf} = TS^{surf} - \Pi V^f + \gamma_p A + \mu N^{surf} \tag{31}$$

by virtue of Euler's homogenous function theorem. Note that Eq. (25), although equivalent to (26), cannot be used to derive U^{surf} because $U^{surf}(\lambda S^{surf}, \lambda h, \lambda A, \lambda N^{surf}) = U^{surf}(\lambda S^{surf}, \lambda^2 V^f, \lambda A, \lambda N^{surf})$ which is not equal to the right-hand side of Eq. (30). Substituting Eq. (29) into Eq. (31) gives:

$$U^{surf} = TS^{surf} + \gamma A + \mu N^{surf} \tag{32}$$

It is noted that Eqs. (16) and (32) share the same expression, despite the former is derived for meso/macropores and the latter is for micropores. This means that surface energy γ preserves its

original definition $\gamma = (\partial U^{surf} / \partial A)_{S,N}$ regardless of the pore size. Subtracting Eq. (25) from the total derivative of Eq. (32) and considering isothermal condition gives:

$$d\gamma = -\Gamma d\mu - \frac{1}{2}\Pi dh \tag{33}$$

Eq. (33) can be viewed as the generalized Gibbs isotherm for micropores. It states that the surface energy for micropores can be modified by altering the chemical potential of the adsorbate as well as the pore size (i.e. $\gamma = \gamma(\mu, h)$). Examining the Maxwell relation of Eq. (33) gives:

$$\left(\frac{\partial \Pi}{\partial \mu}\right)_h = 2\left(\frac{\partial \Gamma}{\partial h}\right)_\mu \tag{34}$$

Differentiating Eq. (29) with respect to μ and substituting Eqs. (33) and (34) gives:

$$\left(\frac{\partial \gamma_p}{\partial \mu}\right)_h = -\Gamma + h\left(\frac{\partial \Gamma}{\partial h}\right)_\mu \tag{35}$$

Using $d\mu = RTd(\ln p)$, the integration of Eqs. (34) and (35) with respect to p yields the final expressions of the surface force terms:

$$\Delta\Pi(p,h) = \Pi(p,h) - \Pi_0(h) = 2RT\int_0^p \frac{1}{p}\frac{\partial \Gamma(p,h)}{\partial h}dp \tag{36}$$

$$\Delta\gamma_p(p,h) = \gamma_p(p,h) - \gamma_{p0}(h) = 2RT\int_0^p \frac{1}{p}\left[-\Gamma(p,h) + h\frac{\partial \Gamma(p,h)}{\partial h}\right]dp \tag{37}$$

where $\Pi_0(h) = \Pi(p=0,h)$ and $\gamma_{p0}(h) = \gamma_p(p=0,h)$ are the reference values of Π and γ_p in vacuum, respectively; $R =$ 8.314 J/mol·K is the ideal gas constant; T is absolute temperature. Eqs. (36) and (37) shows that the adsorption-induced variations of Π and γ_p are completely determined once the adsorption isotherm $\Gamma(p,h)$ is given. Physically, the adsorbate molecules can be thought of as a probe in detecting the potential fields near pore surfaces at the given geometry, and the result of which is collected in the observed adsorption data $\Gamma(p,h)$. Eqs. (36) and (37) serve the important role of recovering the surface force information from $\Gamma(p,h)$, which is the key to quantify solid-adsorbate interaction induced by adsorption. Eqs. (36) and (37) are fundamental to our development as they do not

311 introduce additional model parameters and are rigorously derived from analysing the energetics of a slit
312 pore. Now examine the asymptotic behaviours of Eqs. (36) and (37) for pore size $h \to \infty$. With
313 increasing h, Γ must become independent of h (i.e. $\lim_{h\to\infty} \partial\Gamma / \partial h = 0$ or a stronger condition
314 $\lim_{h\to\infty} h \cdot \partial\Gamma / \partial h = 0$) as soon as the opposing adsorbed regions cease to overlap (i.e. the case of free
315 adsorption). Substituting this into Eqs. (36) and (37) and considering Eq. (29) immediately indicates that
316 disjoining pressure vanishes ($\Pi = \Pi_0(\infty) = 0$) and the equivalent surface tension approaches the surface
317 energy ($\gamma_p = \gamma$) when $h \to \infty$. Also Eq. (33) reduces to the classical Gibbs' isotherm $d\gamma = -\Gamma d\mu$.
318 These asymptotes are indeed consistent with the previous derivations for larger pores (Zhang, 2018).
319 Thus, we conclude that Eqs. (36) and (37) remain valid regardless of pore size and elegantly unify the
320 surface forces active in micro- and meso/macro- pores.

321 *3.2 CONSTRAINED ADSORPTION IN A SLIT PORE*

322 Given the important role that the adsorption isotherm plays in determining the surface forces, the
323 selection of a physically sound expression for $\Gamma(x,h)$ is crucial to our development. Both the Langmuir
324 isotherm (Langmuir, 1918) and the BET isotherm (Brunauer et al., 1938) describe adsorption on free
325 surfaces which might be suitable only for meso/macro porous materials (Gor and Bernstein, 2016;
326 Vandamme et al., 2010; Zhang, 2018; Zhao et al., 2014). Adsorption in micropores is drastically
327 different in the sense that it is constrained by the geometry and size of the pores. Brunauer et al. (1940)
328 have tackled this problem by considering an upper and lower adsorption surface, and applied the
329 statistical rules that are used to derive the BET theory to describe the filling process of a single slit pore
330 upon increasing fluid pressure (Fig. 3). Their adsorption model is known as the BDDT model
331 (Campagnolo and Akgerman, 1995; Müller et al., 1989) and extends the BET model to capture
332 isotherms of type IV and V. Nguyen et al. (2019) have extended the BET theory to study laterally
333 constrained adsorption to represent adsorption in relatively complex pore networks, which improves the
334 predictions of the BET theory for isotherms of type I, II, and III. A detailed review of other adsorption
335 models proposed over the years can be found in Dąbrowski (2001). Among the aforementioned works,
336 only the BDDT model has explicit dependence on the pore size *h* and at the same time is derived for slit
337 pore geometry which is consistent with our pore-scale analysis. We thus choose this model to represent
338 micropore adsorption and to derive the corresponding surface forces. The BDDT model (Brunauer et al.,
339 1940) can be written as:

$$\frac{\Gamma(x,n)}{\Gamma_0}=\frac{cx}{1-x}\cdot\left\{\frac{1+\left(\frac{ng}{2}-n\right)x^{n-1}-(ng-n+1)x^{n}+\frac{ng}{2}x^{n+1}}{1+(c-1)x+\left(\frac{cg}{2}-c\right)x^{n}-\frac{cg}{2}x^{n+1}}\right\} \tag{38}$$

In writing Eq. (38), we have assumed that $\Gamma/\Gamma_0 = V_{adsorbed}/V_0$ with $V_{adsorbed}$ and V_0 denoting the total adsorbed volume and the single-layer volume of adsorbate; Γ_0 is a reference excess concentration with units of moles per unit area; $x = p/p_{sat}$ is the ratio of gas pressure over the saturation pressure; n is the maximum number of adsorbed layers that can fit between the two surfaces, which can be interpreted as a dimensionless pore size; c and g can be expressed in terms of physical quantities as $c \approx \exp(\Delta E/(RT))$ and $g = \exp(Q/(RT))$ (Brunauer et al., 1940; Brunauer et al., 1938); ΔE is the difference between the energy to bond a fluid layer to a solid surface and the energy to bond a fluid layer to a fluid layer; Q is the additional heat necessary to place the last layer of molecules between the two adsorbed surfaces. ΔE and Q will be referred to as the *adsorption energy* and the *additional adsorption heat* hereafter. It should be noted that the additional adsorption heat must be in the range of $0 < Q < 2\gamma S$ (Brunauer et al., 1940) where S is the area occupied by one mole of adsorbate in a complete mono-layer. Setting $n = 1$ and $x \to \infty$ in Eq. (38) gives $\Gamma = N/A = \Gamma_0$, the inverse of which is essentially $S = A/N = 1/\Gamma_0$. Thus, the range of Q becomes $0 < Q < 2\gamma/\Gamma_0$ for the current form of BDDT. This condition is checked throughout this paper to ensure consistency with Brunauer et al. (1940). It is also worth mentioning that Eq. (38) is the simplified version of the BDDT theory where the adsorbed layers are assumed to meet at the middle of the pore. The more comprehensive version that removed such assumption has the same number of parameters and gives similar qualitative trends on the adsorption isotherm. It is however more mathematically cumbersome for the subsequent derivations and demonstrations of the basic working mechanisms of the model.

The typical shape of Eq. (38) is visualized in Fig. 3. The model captures that for very small pores (low n values), adsorption occurs rapidly at low gas pressures and quickly reaches saturation, resembling type-I adsorption. For large pores (high n values), the isotherm reaches a plateau first and then gradually ramps up as pressure increases similar to type-II adsorption. For intermediate pores (medium n), the model exhibits two plateaus like a type-IV adsorption isotherm. Physically, the plateau at low pressure corresponds to the filling of the first layer and the other at high pressure corresponds to

the saturation of the pore. Overall, the increase of pore size through n enhances the total adsorption capacity of the pore, as expected. Another perspective is to look at the adsorption vs. n relation at constant pressures. The theory predicts that the amount of adsorption increases and then decreases with respect to decreasing n at low pressures. This corresponds well with physical intuition: the reduced distance between the two adsorbing walls can enhance the intensity of the attractive potential and thus boost the total adsorption, while further reducing pore space tends to squeeze the molecules out and thus reduce the adsorbed amount (Gor et al., 2017).

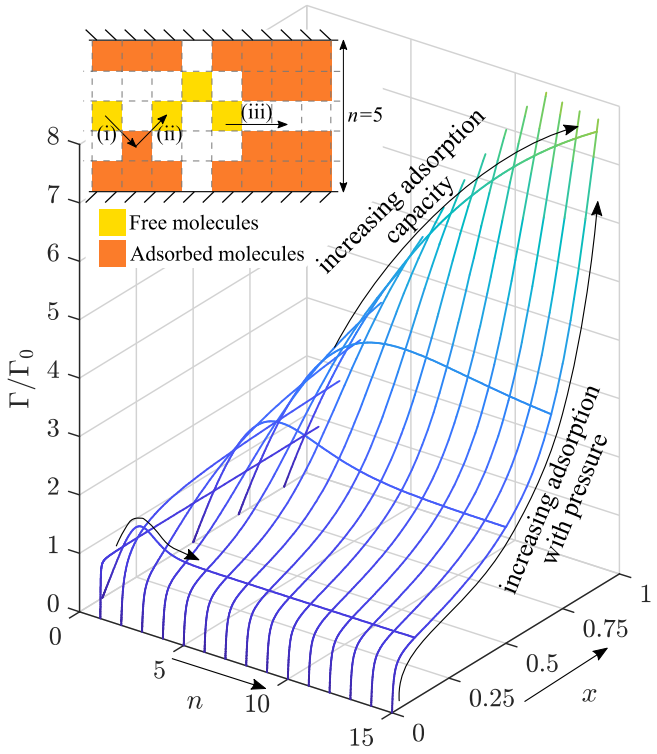

Fig. 3. The BDDT adsorption isotherm for $\Delta E = 757\text{cal/mol}$ and $Q = 440\text{cal/mol}$ at $T = 76\text{K}$. Subfigure shows the statistical model used to derive the BDDT isotherm for slit pores (modified from Brunauer et al., 1940). In the figure the arrows represent (i) adsorption/condensation, (ii) desorption/evaporation, and (iii) bonding of molecular layer to two layers of molecules which requires an additional energy, Q, to that of adsorption to a single layer.

Now let us generate the surface force isotherms based on the BDDT adsorption model. Assume a linear relation between the maximum number of adsorbed layers n and the slit pore size h

$$n = C_h h \tag{39}$$

where $1/C_h$ is the height of each layer which is further related to the size of the adsorbate molecule.

Combining Eqs. (38) and (39) gives

383 $$\frac{\partial \Gamma}{\partial h}=\frac{\Gamma_0 C_h c}{(1-x)C_3^2}\left[C_1\left(1+(c-1)x+C_2x^n\right)x^n+\left\{C_1 n+\left(C_1 n(c-1)-C_2-1\right)x-(c-1)x^2\right\}x^n\ln x\right] \quad (40)$$

384 where the coefficients are $C_1(g,x)=(gx^2-2gx+2x+g-2)/2$, $C_2(c,g,x)=c(g-gx-2)/2$, and
385 $C_3(c,g,x,n)=1+(c-1)x+C_2x^n$. It can be readily shown from Eq. (40) that the BDDT theory satisfies
386 the asymptotic condition of $\lim_{h\to\infty} h\cdot\partial\Gamma/\partial h=0$ and thus can give a unified surface force model as
387 discussed earlier. Substituting Eqs. (38) and (40) into Eqs. (36) and (37), the computed dimensionless
388 disjoining pressure $\Delta\tilde{\Pi}(x,n)=\Delta\Pi/2RT\Gamma_0C_h$ and equivalent surface tension $\Delta\tilde{\gamma}_p(x,n)=\Delta\gamma_p/2RT\Gamma_0$
389 for different Q values are plotted in Fig. 4. The parameters are adapted from nitrogen adsorption at
390 $T=76\text{K}$ reported in (Brunauer et al., 1940). The integrations in Eqs. (36) and (37) are performed using
391 a lower Reimann integration scheme (Appendix A). It is observed that higher adsorption energy Q
392 boosts the amount of adsorption at small pore sizes and large pressure levels. It also enhances the
393 attractive disjoining pressure at low pressure regimes. On the other hand, the equivalent surface tension
394 $\Delta\tilde{\gamma}_p$ monotonically decreases with respect to pressure regardless of the value of Q. Comparison of $\Delta\tilde{\Pi}$
395 and $\Delta\tilde{\gamma}_p$ isotherms implies that the two terms indeed create a competing effect in driving the
396 deformation of the porous material, i.e. negative $\Delta\tilde{\Pi}$ implies attraction and thus shrinkage while
397 negative $\Delta\tilde{\gamma}_p$ implies surface relaxation and thus swelling of the porous skeleton. Their relative
398 dominance on the overall deformation of microporous media upon adsorption shall be quantitatively
399 studied by integrating this pore-scale model with a continuum theory in the following section.

400 Fig. 5 extends the normalized disjoining pressure isotherm in Fig. 4 along the third axis, pore size n,
401 for parameters $\Delta E=757\text{cal/mol}$ and $Q=280\text{cal/mol}$ at $T=76\text{K}$. The model predicts that the change
402 of disjoining pressure is significant for micropores but gradually diminishes for large pores. Strong
403 attractive disjoining pressure presents in small pores at low pressures but is gradually neutralized as pore
404 size and pressure increases. At large pressure levels, only repulsive $\Delta\tilde{\Pi}$ is predicted for all pore sizes.
405 The qualitative attraction-repulsion trend of the disjoining pressure predicted by the model is similar to
406 that observed through Molecular Dynamics (MD) simulations (Kowalczyk et al., 2008).

407

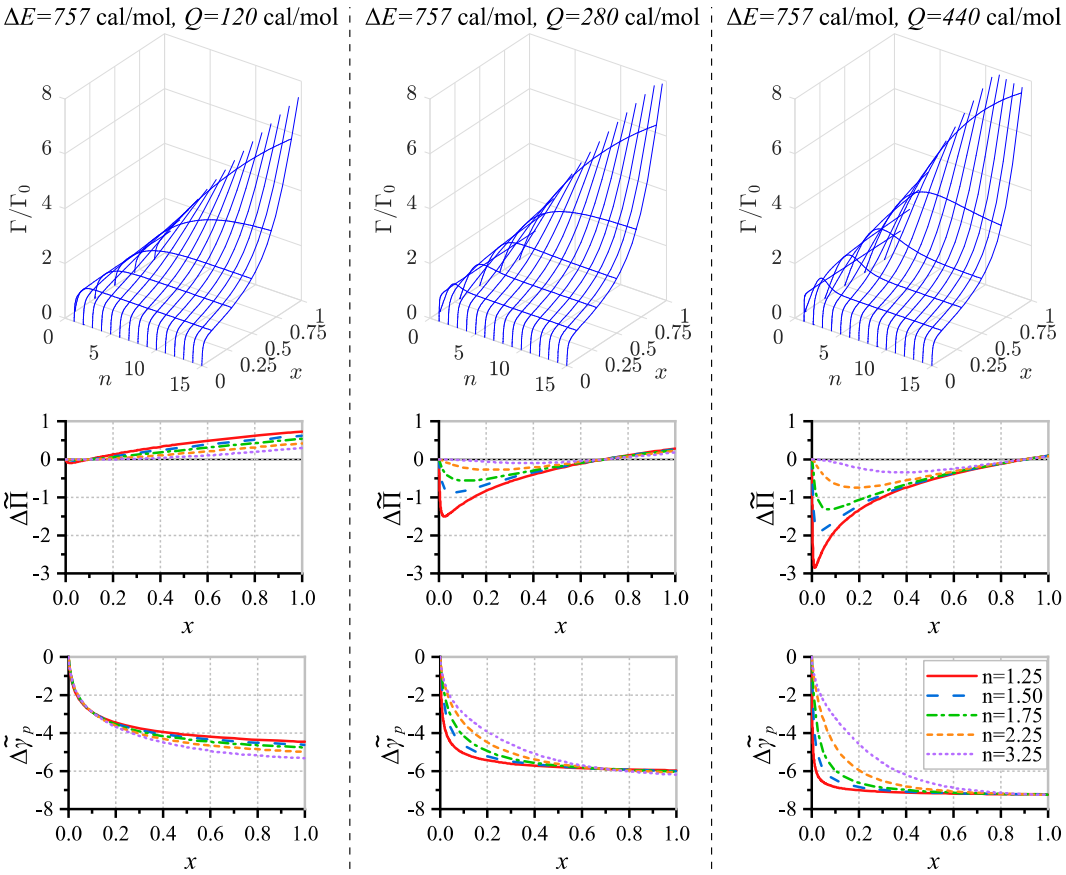

Fig. 4. Predicted disjoining pressure and surface tension isotherms based on the BDDT theory

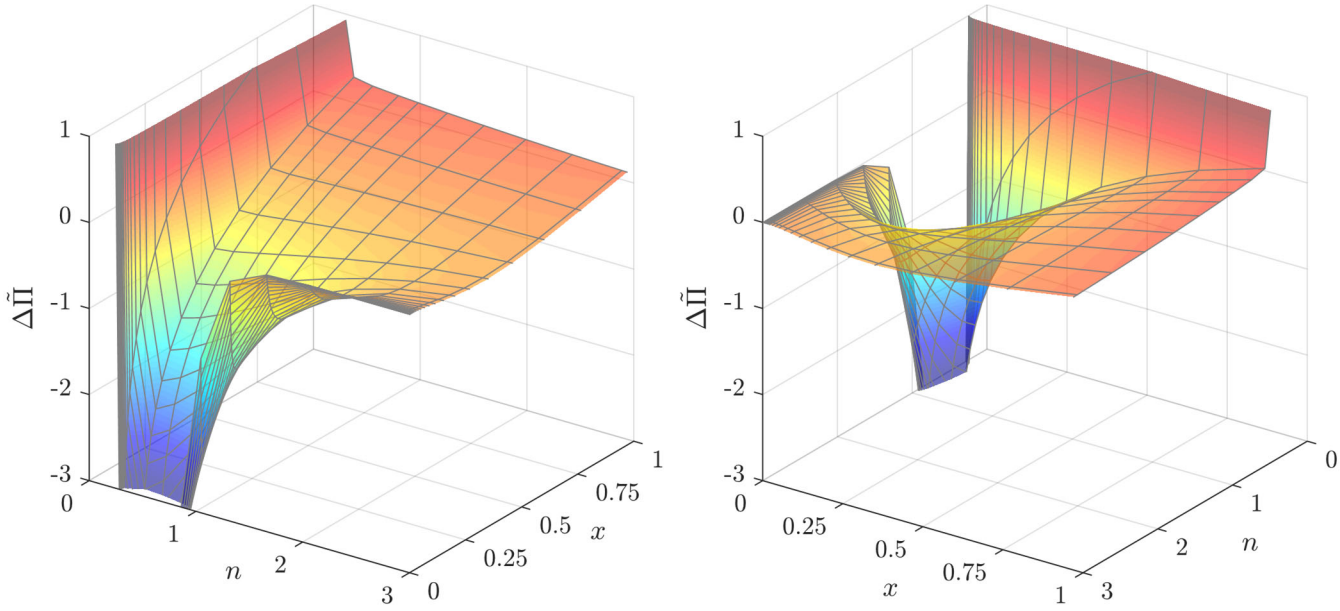

Fig. 5. Disjoining pressure surface viewed at different angles for $\Delta E = 757\text{cal/mol}$ and $Q = 280\text{cal/mol}$ at $T = 76\text{K}$.

4 CONSTITUTIVE LAWS FOR SORPTIVE MICROPOROUS MEDIA

4.1 FREE ENERGY BALANCE

Let us now revisit the system in Fig. 1 to upscale the single-pore surface forces into equivalent stresses or pressures in a microporous continuum. Assuming the material consists of mono-size slit pores, Eq. (24) remains valid and represents the free energy of the total surface phase in a chemically and thermally equilibrated system. Converting all the extensive properties to intensive properties and replacing respectively the pore volume dV^f and surface area dA with $d\Omega^v = d(\phi\Omega_0)$ and $d\mathcal{A} = d(A_s\Omega_0)$, Eq. (24) can be rewritten as

$$d\psi^{surf} = -s^{surf}dT + \mu d\Gamma - \Pi\frac{1}{A_s}d\phi + \left(\gamma_p + \mu\Gamma - \psi^{surf}\right)\frac{1}{A_s}dA_s + \frac{1}{\Omega_0}\left(\gamma_p + \mu\Gamma - \psi^{surf} - \Pi\frac{\phi}{A_s}\right)d\Omega_0 \quad (41)$$

where ψ^{surf} and s^{surf} are the area-specific surface free energy and entropy defined by $F^{surf} = \psi^{surf}\mathcal{A}$ and $S^{surf} = s^{surf}\mathcal{A}$, respectively. Eq. (41) must be valid for arbitrary change of the material volume $d\Omega_0$, thus the last term on the right-hand side must vanish, giving:

$$\psi^{surf} = \gamma_p + \mu\Gamma - \Pi\left(\frac{\phi}{A_s}\right) \quad (42)$$

Substituting Eq. (42) into (41) yields:

$$d\psi^{surf}\left(T,\Gamma,\phi/A_s\right) = -s^{surf}dT + \mu d\Gamma - \Pi d\left(\frac{\phi}{A_s}\right) \quad (43)$$

To derive the material dissipation of each phase, the system's Helmholtz energy may be decomposed as $\Psi = \Psi^s + \Psi^{surf} + \Psi^f = (J-\varphi)\psi^s + A_s\psi^{surf} + \varphi\psi^f$ similar to E and S. The volume/area specific quantities can be made compatible with Eq. (12) by converting to mass-specific ones through $\psi^s = \rho^s\hat{\psi}^s$, $\psi^{surf} = \rho^{surf}\hat{\psi}^{surf}$, $\psi^f = \rho^f\hat{\psi}^f$, $s^{surf} = \rho^{surf}\hat{s}^{surf}$, $s^f = \rho^f\hat{s}^f$, and $\mu^f = M\hat{\mu}^f$. By observing Eq. (43) and considering the above, the new decomposition of material dissipation Eq. (12) for microporous solid is proposed as follows:

$$\Phi_M^s = \mathbf{S}:\frac{\partial\mathbf{E}}{\partial t} + \left(p+\Pi\right)\frac{\partial\phi}{\partial t} - S^s\frac{\partial T}{\partial t} - \left(\rho^{surf}\hat{\psi}^{surf} - M\hat{\mu}^f\Gamma + \Pi\frac{\phi}{A_s}\right)\frac{\partial A_s}{\partial t} - \frac{\partial\rho^s\left(J-\phi\right)\hat{\psi}^s}{\partial t} \quad (44)$$

$$\Phi_M^{surf} = A_s\left[M\hat{\mu}^f \frac{\partial \Gamma}{\partial t} - \rho^{surf}\hat{s}^{surf}\frac{\partial T}{\partial t} - \Pi\frac{\partial}{\partial t}\left(\frac{\phi}{A_s}\right) - \frac{\partial \rho^{surf}\hat{\psi}^{surf}}{\partial t}\right] \tag{45}$$

$$\Phi_M^f = \rho^f\phi\left[-p\frac{\partial}{\partial t}\left(\frac{1}{\rho^f}\right) - \hat{s}^f\frac{\partial T}{\partial t} - \frac{\partial \hat{\psi}^f}{\partial t}\right] \tag{46}$$

One can verify that the summation of Eqs. (44) through (46) recovers Eq. (12). Eq. (46) is identical to the fluid part of the material dissipation presented in Zhang (2018) and thus embodies the standard state equations of a bulk fluid mixture (DeHoff, 2006). Setting $\Phi_M^{surf} = 0$ in Eq. (45) also gives exactly the surface free energy balance of a microporous network as in Eq. (43). We are thus left with Eq. (44) to explore the constitutive response of a sorptive microporous media. Substituting Eq. (42) into (44) and considering a reversible process ($\Phi_M^s = 0$) gives the free energy balance of the solid phase:

$$d\Psi^s = \mathbf{S} : d\mathbf{E} + \left(p + \Pi\right)d\phi - S^s dT - \gamma_p dA_s \tag{47}$$

It is readily observed that, for microporous solid, the thermodynamic force conjugated to porosity change becomes the bulk fluid pressure *p* shifted by the disjoining pressure Π, and the surface tension conjugated to change of surface area is also modified from γ to γ_p. These are consistent with our conclusions from pore-scale analysis (i.e. Eq. (27)). Note that Π and γ_p in Eq. (47) should be the smeared value of disjoining pressure and surface tension in all pores if multiple pore sizes exist (See for example Appendix C). For large pores, we have shown that $h \to \infty$, $\Pi \to 0$ and $\gamma_p \to \gamma$, thus Eq. (47) reduces to:

$$d\Psi^s = \mathbf{S} : d\mathbf{E} + pd\phi - S^s dT - \gamma dA_s \tag{48}$$

which has been exactly derived for meso/macro porous media (Zhang, 2018). The current enrichment therefore enables the surface poromechanics framework to model materials with pores of micro to macro sizes. Note that if the dependency of surface energy on the surface deformation is to be considered, γ should be replaced by the surface stress defined by Shuttleworth (1950).

4.2 Model specialization

The application of Eq. (48) for finite-strain deformation, multi-species adsorption and two-way coupled adsorption-deformation for mesoporous media has been previously explored by Zhang (2018).

Here we shall constrain the discussion to small-strain and isothermal condition to focus more on the new physics introduced by micropores. Eq. (47) then reduces to:

$$d\Psi^s = \sigma d\varepsilon + \mathbf{s} : d\mathbf{e} + \left(p + \Pi \right) d\phi - \gamma_p dA_s \tag{49}$$

where ε and $\mathbf{e}$ are the volumetric and deviatoric part of the infinitesimal strain tensor, respectively; σ and $\mathbf{s}$ are the mean and deviatoric part of the Cauchy stress tensor, respectively. Considering the specific surface area of the REV evolves with its porosity and strain (i.e $A_s(\phi, \varepsilon, \mathbf{e})$), Eq. (49) becomes:

$$d\Psi^s = \left(\sigma - \gamma_p \frac{\partial A_s}{\partial \varepsilon} \right) d\varepsilon + \left(\mathbf{s} - \gamma_p \frac{\partial A_s}{\partial \mathbf{e}} \right) : d\mathbf{e} + \left(p + \Pi - \gamma_p \frac{\partial A_s}{\partial \phi} \right) d\phi \tag{50}$$

For the simple case of linear isotropic poroelastic skeleton, one can specify:

$$\Psi^s(\varepsilon, \mathbf{e}, \phi) = \frac{1}{2}\left(K + b^2 N \right)(\varepsilon - \varepsilon_r)^2 - bN(\varepsilon - \varepsilon_r)\left(\phi - \phi_r \right) + \frac{1}{2} N \left(\phi - \phi_r \right)^2 + G\left(\mathbf{e} - \mathbf{e}_r \right) : (\mathbf{e} - \mathbf{e}_r) \tag{51}$$

where K and G are the bulk and shear moduli, respectively; b and N are Biot's coefficient and Biot's modulus, respectively; and $(\varepsilon_r, \mathbf{e}_r, \phi_r)$ is an arbitrary reference state for the REV. Substituting (51) into (50) gives:

$$\begin{cases} \sigma - \sigma_a = \left. \dfrac{\partial \Psi^s}{\partial \varepsilon} \right|_{\phi, \mathbf{e}} = \left(K + b^2 N \right)(\varepsilon - \varepsilon_r) - bN\left(\phi - \phi_r \right) \\ p - p_a = \left. \dfrac{\partial \Psi^s}{\partial \phi} \right|_{\varepsilon, \mathbf{e}} = -bN(\varepsilon - \varepsilon_r) + N\left(\phi - \phi_r \right) \\ \mathbf{s} - \mathbf{s}_a = \left. \dfrac{\partial \Psi^s}{\partial \mathbf{e}} \right|_{\varepsilon, \phi} = 2G\left(\mathbf{e} - \mathbf{e}_r \right) \end{cases} \tag{52}$$

where

$$\sigma_a = \gamma_p \frac{\partial A_s}{\partial \varepsilon},\ p_a = \gamma_p \frac{\partial A_s}{\partial \phi} - \Pi \text{ and } \mathbf{s}_a = \gamma_p \frac{\partial A_s}{\partial \mathbf{e}} \tag{53}$$

are the stress components induced by adsorption and are referred to as the *adsorption stresses*. Apparently, such stresses for microporous solid Eq. (53) differs from those for meso/macro porous solid Eq. (1) by the presence of Π and γ_p.

We shall define the reference state in such a way that facilitates the calibration of the model based on routine experiments. Observing Eqs. (36) and (37), the adsorption stresses may be written as

$$\sigma_a = \sigma_{a0} + \Delta\sigma_a,\ p_a = p_{a0} + \Delta p_a \text{ and } \mathbf{s}_a = \mathbf{s}_{a0} + \Delta\mathbf{s}_a \tag{54}$$

with $\sigma_{a0} = \gamma_{p0}\left(\partial A_s / \partial\varepsilon\right)\big|_{\boldsymbol{\varepsilon}=\mathbf{0},\phi=\phi_0}$, $p_{a0} = -\Pi_0 + \gamma_{p0}\left(\partial A_s / \partial\phi\right)\big|_{\boldsymbol{\varepsilon}=\mathbf{0},\phi=\phi_0}$, $\mathbf{s}_{a0} = \gamma_{p0}\left(\partial A_s / \partial\mathbf{e}\right)\big|_{\boldsymbol{\varepsilon}=\mathbf{0},\phi=\phi_0}$ and

$$\Delta\sigma_a = \Delta\left(\gamma_p \frac{\partial A_s}{\partial\varepsilon}\right),\ \Delta p_a = \Delta\left(\gamma_p \frac{\partial A_s}{\partial\phi}\right) - \Delta\Pi \text{ and } \Delta\mathbf{s}_a = \Delta\left(\gamma_p \frac{\partial A_s}{\partial\mathbf{e}}\right) \tag{55}$$

where ϕ_0 is the initial porosity; symbol Δ denotes the difference between the current value and initial value of its operand. By taking the reference state as:

$$\begin{cases} \sigma_{a0} = \left(K + b^2 N\right)\varepsilon_r - bN\left(\phi_r - \phi_0\right) \\ p_{a0} = -bN\varepsilon_r + N\left(\phi_r - \phi_0\right) \\ \mathbf{s}_{a0} = 2G\mathbf{e}_r \end{cases} \tag{56}$$

and combining Eqs. (54), the constitutive law Eq. (52) can be simplified into

$$\begin{cases} \sigma - \Delta\sigma_a = \left(K + b^2 N\right)\varepsilon - bN\left(\phi - \phi_0\right) \\ p - \Delta p_a = -bN\varepsilon + N\left(\phi - \phi_0\right) \\ \mathbf{s} - \Delta\mathbf{s}_a = 2G\mathbf{e} \end{cases} \tag{57}$$

The advantage of Eq. (57) over Eq. (52) is that the material starts with zero initial strain ($\varepsilon = 0$, $\mathbf{e} = \mathbf{0}$) and a given initial porosity $\phi = \phi_0$ under vacuum ($\Delta\sigma_a = \Delta p_a = 0$ and $\Delta\mathbf{s}_a = \mathbf{0}$) and stress-free ($\sigma = p = 0$ and $\mathbf{s} = \mathbf{0}$) condition, which is consistent with most adsorption-deformation experiments (Balzer et al., 2015; Hol and Spiers, 2012). From a poromechanics perspective, Eq. (57) provides a new effective stress definition for sorptive porous solid:

$$\sigma' = \sigma + bp - \left(\Delta\sigma_a + b\Delta p_a\right) \tag{58}$$

as compared to the Biot's effective stress $\sigma' = \sigma + bp$ for non-interactive porous materials.

Finally, a microstructure model $A_s(\phi,\varepsilon,\mathbf{e})$ is necessary to specify the geometrical factors in Eq. (55). Consider a network of spherical pores for this purpose. the surface area-porosity relation is given by (Zhang, 2018):

$$A_s = \frac{3}{R_0}\phi_0^{1/3}\phi^{2/3} \tag{59}$$

where ϕ_0 is the initial porosity and R_0 is the radius of the spherical pore when $\phi = \phi_0$. Note that such a spherical pore model induces an inconsistency with the slit-pore geometry used in pore-scale analysis. To link the slit-pore model with the spherical pore microstructure, it is possible to introduce a mapping parameter α defined by

$$h = \alpha R_0 \tag{60}$$

such that the adsorption behaviour in a sphere of radius R_0 is equivalent to that of a slit pore of width *h*. The mapping parameter α can be taken as 2/3 through simple geometrical considerations (see Appendix B). By writing Eq. (60), we have made the simplification that the equivalent slit pore size is calculated based on the initial spherical pore size R_0 rather than the current one R which is a function of external stress. This choice is made to focus the current study on adsorption-induced deformation rather than the two-way coupling between adsorption and straining which has been already explored in Zhang (2018). The geometrical factors can be finally obtained from Eq. (59):

$$\frac{\partial A_s}{\partial \varepsilon} = 0\,;\ \frac{\partial A_s}{\partial \phi} = \frac{2}{R_0}\left(\frac{\phi_0}{\phi}\right)^{1/3} = C_\phi\,;\ \frac{\partial A_s}{\partial \mathbf{e}} = \mathbf{0} \tag{61}$$

Thus Eq. (55) becomes

$$\Delta\sigma_a = 0\,;\ \Delta p_a = \Delta\left(\gamma_p C_\phi\right) - \Delta\Pi\,;\ \Delta\mathbf{s}_a = 0 \tag{62}$$

Evidently, the effect of adsorption for this special case comes down to a single adsorption stress Δp_a that modifies the pore pressure. Therefore, the competing role of $\Delta\Pi$ and $\Delta\gamma_p$ on the induced deformation can be directly inspected by examine the sign of the dimensionless adsorption pressure $\Delta\tilde{p}_a = \Delta p_a / 2RT\Gamma_0 C_h$. If the reduction of surface tension is greater than the attractive disjoining

pressure, i.e. $-\Delta\left(\gamma_p C_\phi\right) > -\Delta\Pi$ and thus $\Delta\tilde{p}_a < 0$, the solid skeleton feels an enhanced pore pressure per Eq. (58) and thus overall swelling will be observed. Conversely, the REV contracts if the attractive $\Delta\Pi$ dominates with $\Delta\tilde{p}_a > 0$. The line drawn by $\Delta\tilde{p}_a = 0$ therefore divides the dimensionless pore size n and dimensionless pressure x space into a contraction domain and a swelling domain, making it a "phase diagram" for adsorption-induced deformation as shown in Fig. 6. Particularly, the model predicts that only materials with sufficiently small pores (i.e. 1~2 adsorbate diameters) at sufficiently low gas pressures (i.e. less than 1% of the saturation pressure) exhibit contraction upon adsorption, which nicely agrees with existing experimental evidence (Balzer et al., 2015; Lakhanpal and Flood, 1957; Yakovlev et al., 2004). Further, the size and shape of the contraction domain is predicted to depend on the solid-fluid interaction characteristics. For example, larger additional adsorption heat Q meaning stronger energy potential between the opposing adsorbed layers motivates a larger contraction regime.

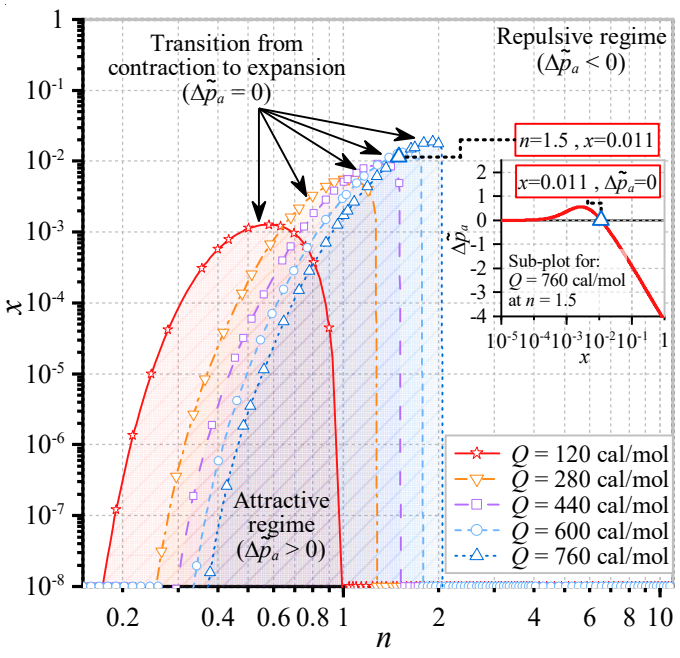

Fig. 6. Adsorption induced contraction-swelling "phase diagram". The curves represent the transition from contractive to expansive behaviour while the shaded areas indicate the contraction regime. The subplot explains how the phase diagram was obtained from a multitude of simulations, each at a certain fixed n value.

5 MODEL PERFORMANCE

5.1 PREDICTED ADSORPTION-DEFORMATION BEHAVIOURS

The constitutive relation Eq. (57), the adsorption stress for spherical pores Eq. (62), and the surface force terms Eqs. (36) and (37) complete the proposed adsorption-deformation model for microporous

536 solids with a total of eight model parameters (K, ν, b, N, ΔE, Q, C_h, and Γ_0). The model also takes
537 the information of the initial microstructure of the specimen via ϕ_0 and R_0 which can be determine by
538 Scanning Electron Microscope (SEM) images or other methods. Inputs of the molar volume of the
539 adsorbate V_m and the specific gravity of the solid G_s are necessary to convert the amount of adsorbed
540 substance Γ from moles per pore surface area to grams per volume of solid. The saturated pressure p_0
541 of the adsorbate is required for the BDDT model. These common numbers (V_m, G_s, p_0) can be
542 referenced from existing mineral and species databases. Since this model uses a single characteristic
543 pore size R_0 to represents the overall pore network, we may refer it to as the *mono-pore model*.

544 Fig. 7 presents the typical adsorption and deformation curves predicted by the model in unjacketed
545 gas pressurization tests (i.e. $\sigma = -p$, $\mathbf{s} = \mathbf{0}$, $p = p$). Four parameters ΔE, Q, R_0 and C_h are varied in
546 this parametric study because they are identified to dominating the mode of the deformation isotherms
547 specifically on the shrinkage-swelling transition. Fig. 7a shows that the adsorption energy ΔE mainly
548 controls the magnitude of swelling strain and has a less significant role in the initial contraction portion.
549 Fig. 7b suggests that the initial contraction is controlled by the additional adsorption heat Q but it does
550 not affect much the overall swelling at large pressures. This can be explained by the fact that higher Q
551 implies stronger interaction between the opposing adsorbed regions and stronger contraction at low
552 pressure regime (see Fig. 4), while ΔE characterises the gas-wall interactions which is more relevant to
553 the surface energy and thus the Bangham expansion portion. On the other hand, parameters R_0 and C_h
554 control the size of the pore and the adsorbate molecules. If less molecules can fit between the pore walls,
555 the adsorption isotherm operates at lower n values which, according to Fig. 5, amplifies the attractive
556 disjoining pressure. This is expected to produce stronger initial contractions which is indeed reflected
557 through decreasing R_0 in Fig. 7c. Similar effect is observed when C_h decreases. It is noted that
558 regardless of the magnitude of the initial contractive strain, the volumetric strain is always predicted to
559 be swelling at high pressure levels, consistent with experimental observations (Balzer et al., 2015;
560 Lakhanpal and Flood, 1957; Yakovlev et al., 2004). For the selected parameters, the adsorption
561 isotherms in Fig. 7 are only subtly varied in contrast to the drastic changes in the volumetric strain
562 responses.

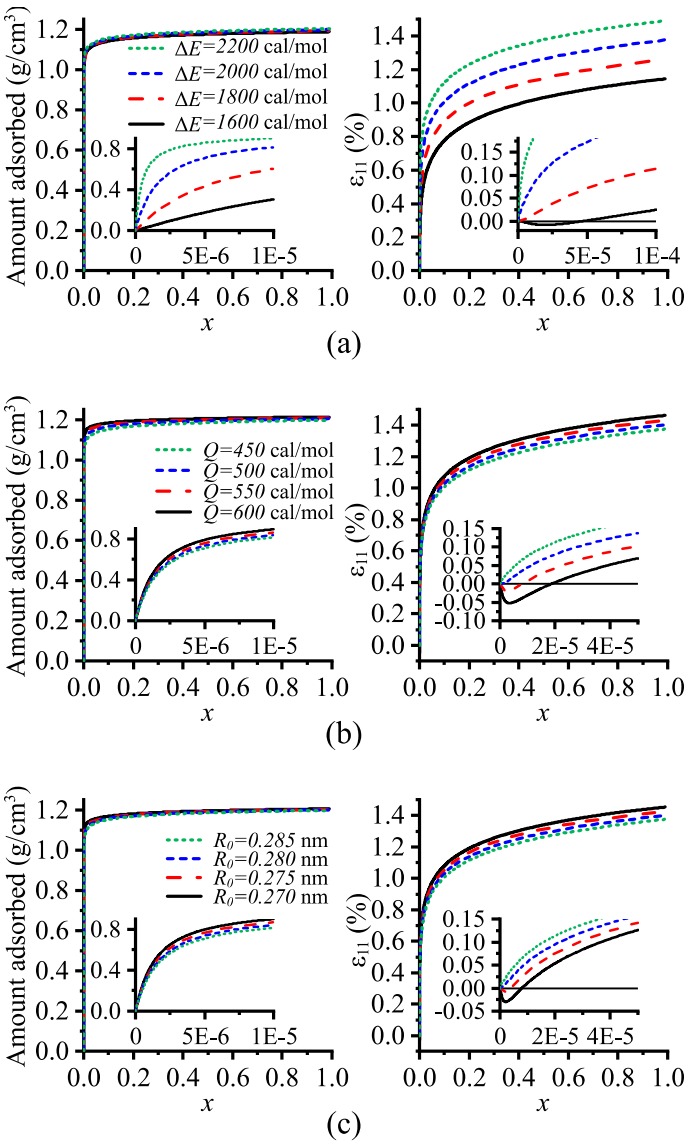

Fig. 7. The effects of (a) ΔE, (b) Q and (c) R_0 on the predicted adsorption and deformation responses. The reference parameters are taken from the BDDT calibration of nitrogen (Brunauer et al., 1940) and the experiment results on nitrogen adsorption on microporous carbon (Balzer et al., 2015): $K = 3.0\text{GPa}$, $\nu = 0.1$, $b = 0.9$, $N = 10\text{GPa}$, $\phi_0 = 0.64$, $\Delta E = 2000\text{cal/mol}$, $Q = 450\text{cal/mol}$, $p_0 = 10\text{kPa}$, $\Gamma_0 = 2.0\text{E-6}\,\text{mol/m}^2$, $C_h = 6.897\,\text{nm}^{-1}$, $R_0 = 0.288\text{nm}$, $V_m = 34\text{cm}^3/\text{mol}$, and $T = 76\text{K}$. The specific gravity of the solid is set as 1.45.

Additional parametric study (not shown here) show that other parameters such as K, ν, b, N, and Γ_0 are mainly to amplify the adsorption or the deformation isotherms rather than to trigger different types of shrinkage-swelling responses. Smaller bulk modulus K represents a softer solid skeleton, thus amplifying both contraction and expansion. Poisson ratio ν has no effect on the prediction in the current setting of isotropic material and unjacketed adsorption. Biot coefficient b has an opposite effect compare to K on the deformation of the solid. Biot modulus N controls the change of porosity and

thus the pore surface area upon fluid pressurization. For the range of porosity changes here, the pore surface area undergoes little changes, making N practically ineffective in the overall prediction. Γ_0 is a direct scaling factor to the amount of adsorption. It also scales the adsorption stresses and the induced deformation.

5.2 MODEL VALIDATION

Balzer et al. (2015) conducted a series of adsorption experiments of CO_2, N_2, and Ar on microporous carbon, all exhibited initial contraction at very low pressures followed by expansion at elevated pressures, which is ideal for validating the proposed model. The sample has a pore structure of interconnected spherical pores with a pore size distribution (PSD) presented in Fig. 8. The PSD shows two peaks, one at pore size of about 18nm and the other at around 0.35nm~0.8nm, suggesting a dual porosity network. Nevertheless, we still use the mono-pore model here to examine the performance of the theory in its simplest form. An improved representation of the pore network, i.e. a dual-pore model will be discussed in the next subsection.

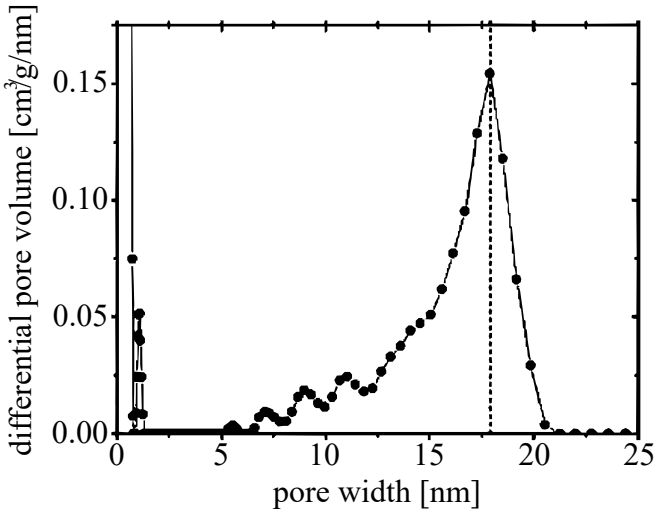

Fig. 8. Pore size distribution of the carbon sample tested by Balzer et al. (2015).

Provided the total pore volume per grams of sample ($0.86\,\mathrm{cm}^3/\mathrm{g}$) and the mass density of the sample ($0.741\,\mathrm{g/cm}^3$), we are able to calculate the porosity of the sample $\phi = 0.637$. The sample particle density $\rho_s = 1.45\mathrm{g/cm}^3$ gives the specific gravity of the solid $G_s = 1.45$. Combining this with the volume of micropores read from Fig. 8 leads to the choice of $R_0 = 1.13\mathrm{nm}$ such that the model has approximately the same specific surface area as the specimen (see Appendix B). Balzer et al. (2011) reported a

595 microporous carbon rod sample with similar porosity to have Young's modulus of about 7.24GPa.
596 Assuming $\nu = 0.1$, the bulk modulus can be calculated as $K = 3\text{GPa}$. The Biot's parameters are chosen
597 as $b = 0.9$ and $N = 10\text{GPa}$ which are within the common ranges for porous carbon (Pijaudier-Cabot et
598 al., 2011; Vandamme et al., 2010). For nitrogen, the molar volume is $V_m^{N_2} = 34\text{cm}^3/\text{mol}$, the saturation
599 pressure is $p_0^{N_2} = 97.2\text{kPa}$ (Lemmon et al.), and its adsorption heat is $Q = 440\,\text{cal/mol}$ at $T = 76\text{K}$
600 calibrated by Brunauer et al. (1940). With the above parameters constrained, we calibrate ΔE, C_h, and
601 Γ_0 to match the experimental data for nitrogen adsorption on microporous carbon (Balzer et al., 2015).
602 Parameters for argon and carbon-dioxide adsorptions are obtained by perturbing adsorption parameters
603 ΔE, Q, C_h, and Γ_0 in the expected directions (Brunauer et al., 1940; Brunauer et al., 1938) with the rest
604 fixed. The molar volume and saturation pressure for argon and carbon-dioxide are $V_m^{Ar} = 28\text{cm}^3/\text{mol}$,
605 $p_0^{Ar} = 70.5\text{kPa}$, $V_m^{CO_2} = 38\text{cm}^3/\text{mol}$, and $p_0^{CO_2} = 3.471\text{MPa}$. The argon adsorption is simulated at the
606 same temperature as the nitrogen adsorption, while the carbon-dioxide adsorption is simulated at
607 $T = 273\text{K}$. The model parameters are summarized in Table 1 and the results are presented in Fig. 9.

608 Table 1. Parameters used in the mono-pore model for N_2, Ar and CO_2 adsorption on porous carbon.

Parameter	Unit	Values		
		N_2	Ar	CO_2
Poroelasticity				
K	[GPa]	3.0	3.0	3.0
ν	[-]	0.10	0.10	0.10
b	[-]	0.9	0.9	0.9
N	[GPa]	10	10	10
Adsorption				
ΔE	[cal/mol]	2090	1800	3100
Q	[cal/mol]	440	460	670
C_h	[1/nm]	1.656	1.704	1.361
Γ_0	[μmol/m^2]	1.905	2.170	0.770
Microstructure				
ϕ_0	[-]	0.64	0.64	0.64
R_0	[nm]	1.13	1.13	1.13

609

610 It can be observed from Fig. 9 that, overall, the mono-pore model can accurately capture the initial
611 contraction and the following expansion for all three gases by keeping the same poromechanical
612 parameters and varying only the adsorption parameters. On the other hand, it is noted that the predicted

adsorption isotherms by a single pore size can only represent the adsorption data at low pressure levels but deviate significantly in the high-pressure regime. We believe that the mismatch of the adsorption isotherms despite the excellent match on the strain isotherms is caused by averaging the pore size distribution (Fig. 8) into a single pore of size R_0. One can see that the smeared pore size $R_0 = 1.13\text{nm}$ is more representative of the micropore network (0.35nm ~ 0.8nm) where the disjoining pressure effects and initial contractions gain dominance. Consequently, adsorption is quickly capped by the small pore size and thus restricting the adsorption amount as gas pressure increases.

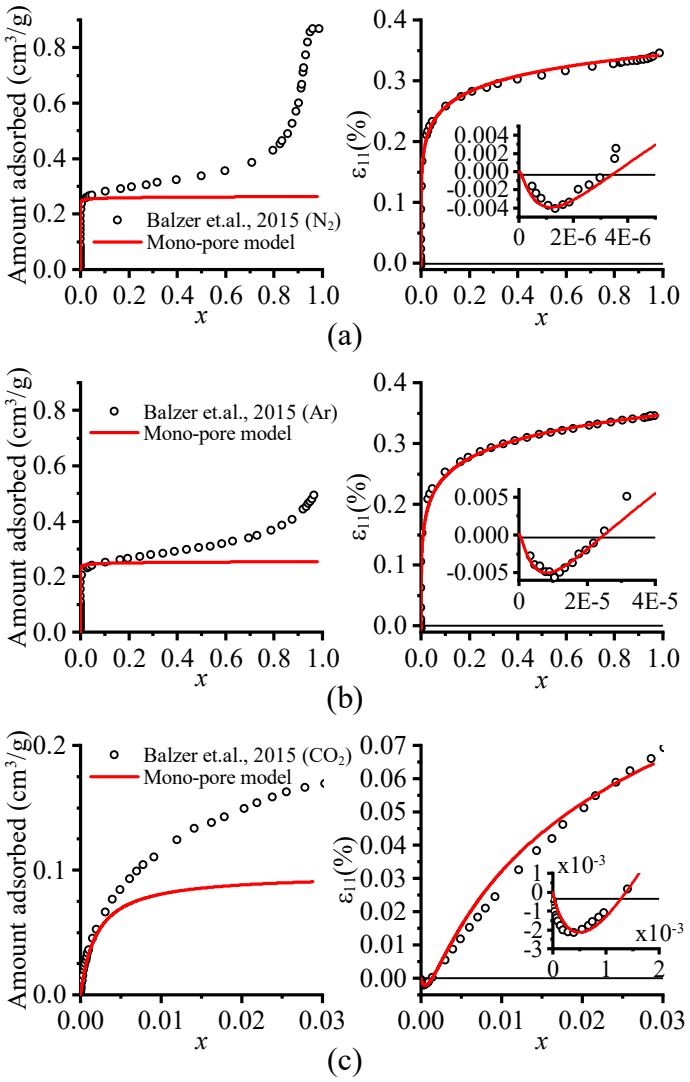

Fig. 9. Mono-pore model vs. experimental data for a) N_2, b) Ar, and c) CO_2 adsorption on microporous carbon.

5.3 *DUAL PORE SIZE APPROACH*

To better distinguish the adsorption-deformation behaviours in the mesoporous and microporous range, we extend the model to incorporate dual pore sizes, which will be referred to as the *dual-pore model*. The initial radius for the two pore sizes are denoted by $R_{1,0}$ and $R_{2,0}$. The volume fractions of different pores with respect to the total pore volume are denoted by r_1 and r_2 with $r_1 + r_2 = 1$. Adsorption in each family of pores is again described by the BDDT model with the corresponding n values. Compared to the mono-pore model, only two new parameters $R_{2,0}$ and r_2 are introduced, both are readily determined from the pore size distribution curve Fig. 8. Details of the model are presented in Appendix C. The performance of the improved model compared against the Balzer et al. (2015)'s data is shown in Fig. 10. The poroelasticity and adsorption parameters are kept the same as in Table 1 and the updated and new parameters for the dual-pore model are listed in Table 2.

Table 2. Updated and new parameters used in the dual-pore model for N_2, Ar and CO_2 adsorption on porous carbon

Parameter	Unit	Values		
		N_2	Ar	CO_2
C_h	[1/nm]	6.452	6.623	5.236
$R_{1,0}$	[nm]	0.288	0.288	0.288
$R_{2,0}$	[nm]	9	9	9
r_1	[-]	0.23	0.23	0.23
r_2	[-]	0.77	0.77	0.77

Fig. 10a and b show that the incorporation of mesopores allows adsorption to continue after the initially rapid filling of the micropores, as expected. Using the same set of adsorption parameters as in the mono-pore model, the dual-pore model well captures the adsorption isotherm at all pressure ranges without sacrificing the level of agreement on the strain isotherms. It is also observed that the adsorbed amounts are slightly overestimated at low pressure ranges and underestimate at higher pressures, which we believe can be resolved by further enriching the pore size descriptors. Fig. 10c, on the other hand, does not show much improvement in comparison with Fig. 9c. A possible reason is that the temperature at which the CO_2 adsorption tests are conducted is significantly different from that of N_2 and Ar, making it difficult to estimate the adsorption energies ΔE and Q. Using the same poroelastic parameters for the case of CO_2 is also questionable because of this temperature difference. Overall, this attempt of model

enhancement shows that improved results can be obtained simply through refinement of the microstructure without adding any new complexity to the theoretical framework. This supports the proposed pore-scale physics that controls the adsorption-deformation coupling in microporous solids.

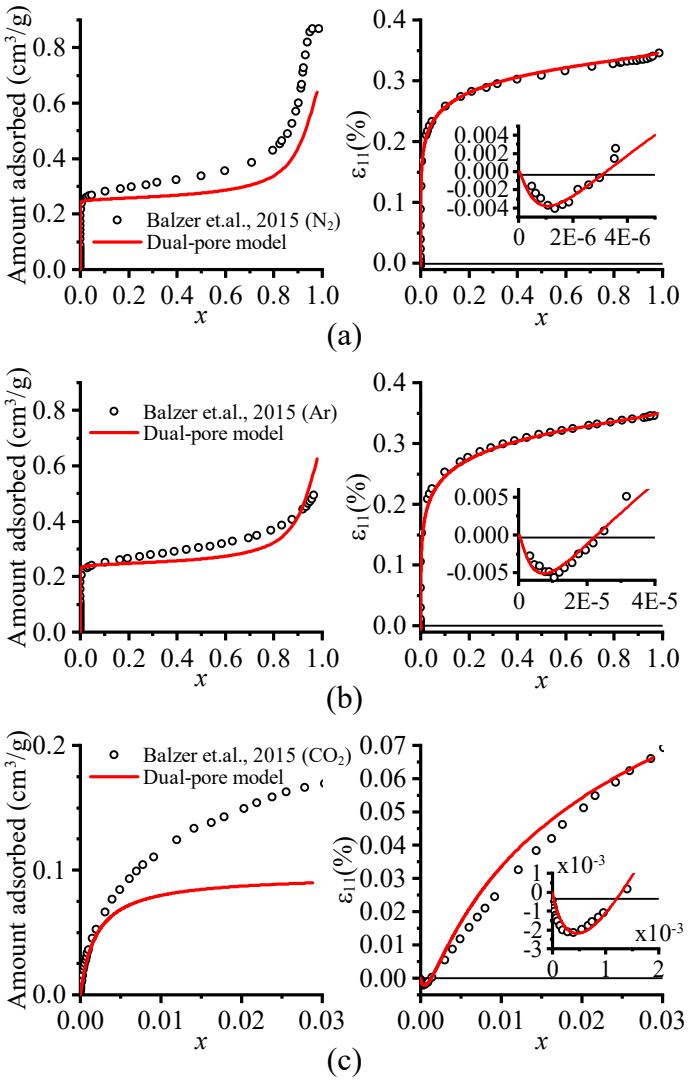

Fig. 10. Dual-pore model vs. experimental data for a) N_2, b) Ar, and c) CO_2 adsorption on microporous carbon.

6 CONCLUSION

This paper generalizes the work of Zhang (2018) for meso/macro porous solids to incorporate the solid-adsorbate interactions in micropores. For the first time, the initial contraction induced by adsorption is quantitatively captured through a continuum approach, as a natural result of upscaling the pore-scale surface forces through rigorous thermodynamics analysis instead of phenomenological

fitting. We start by reviewing the thermodynamics of porous materials saturated by unary adsorptive fluid. The need for a valid decomposition of the overall energy dissipation in microporous media drives us to study the energetics of individual micropores and the constrained adsorption process. We analysed a nano-sized slit pore and considered the extra work induced by the overlapping of the interfacial zones of two opposite pore walls. This gives rise to the disjoining pressure and the modified surface tension, whose competition is proven to determine the shrinkage-swelling transition of the microporous solid upon adsorption. The partitioning of the material dissipation is then performed to reveal the free energy of microporous solid skeleton, where the adsorption stresses is rigorously derived as a function of surface forces and pore morphology. An adsorption-deformation model is finally constructed by specializing linear isotropic poroelasticity, spherical pore geometry, and the BDDT isotherm, and then put to test against recent experimental results. The main conclusions of this study are highlighted below:

1. For microporous solids, disjoining pressure arises in the micropores and, together with the bulk fluid pressure, drives the changes of macroscopic porosity. Such pressure also modifies the surface tension conjugated to the changes of surface area. These terms fundamentally arose from the surface forces between two closely spaced pore walls and play key roles in determining the adsorption-deformation behaviour of microporous solids.

2. The BDDT theory provides a simple and robust adsorption model for slit pores with varying sizes. It produces a rich set of disjoining pressure and surface tension isotherms that reasonably represent the shrinkage-swelling competitions at the early stage of adsorption.

3. The simple mono-pore model can produce a wide spectrum of adsorption-deformation behaviours by only using physically meaningful and experimentally measurable parameters. The model can reasonably capture the deformation of microporous carbons interacting with different gases. The agreement with adsorption data is limited due to the oversimplifying assumption of a single pore size.

4. The incorporation of a dual-size pore structure significantly enhances the model performance. Both adsorption and strain isotherms can be simultaneously captured with only two new parameters without modifying the poromechanical parameters. This supports our theoretical foundation which heavily relies on pore-scale energetics and upscaling.

687 Within the surface poromechanics framework, further improvement of the model can be
688 accomplished by (1) introducing the two-way adsorption-deformation coupling by allowing the pore size
689 to vary as the material deforms, and (2) incorporating a continuous pore size distribution rather than a
690 single or dual pore averaging. Some fundamental aspects also need to be further studied, including the
691 adsorption process and surface forces in spherical pores (as compared to slit pores) as well as the effect
692 of condensation at large gas pressures.

693 ## 7 ACKNOWLEDGEMENT

694 This research was supported by the U.S. Department of Energy through grant DE-NE0008771.

REFERENCES

Amberg, C., McIntosh, R., 1952. A study of adsorption hysteresis by means of length changes of a rod of porous glass. Canadian Journal of Chemistry 30, 1012-1032.

Anand, L., 2015. 2014 Drucker medal paper: A derivation of the theory of linear poroelasticity from chemoelasticity. Journal of Applied Mechanics 82, 111005.

Ash, S.G., Everett, D.H., Radke, C., 1973. Thermodynamics of the effects of adsorption on interparticle forces. Journal of the Chemical Society, Faraday Transactions 2 69, 1256.

Baek, S., Pence, T.J., 2009. On swelling induced degradation of fiber reinforced polymers. International Journal of Engineering Science 47, 1100-1109.

Balzer, C., Braxmeier, S., Neimark, A.V., Reichenauer, G., 2015. Deformation of Microporous Carbon during Adsorption of Nitrogen, Argon, Carbon Dioxide, and Water Studied by in Situ Dilatometry. Langmuir : the ACS journal of surfaces and colloids 31, 12512–12519.

Balzer, C., Wildhage, T., Braxmeier, S., Reichenauer, G., Olivier, J.P., 2011. Deformation of porous carbons upon adsorption. Langmuir : the ACS journal of surfaces and colloids 27, 2553–2560.

Bangham, D., Fakhoury, N., 1928. The expansion of charcoal accompanying sorption of gases and vapours. Nature 122, 681.

Bangham, D., Razouk, u.R., 1938. The saturation and immersion expansions and the heat of wetting. Proceedings of the Royal Society of London. Series A. Mathematical and Physical Sciences 166, 572-586.

Bertinetti, L., Fischer, F., Fratzl, P., 2013. Physicochemical basis for water-actuated movement and stress generation in nonliving plant tissues. Physical review letters 111, 238001.

Biot, M.A., Temple, G., 1972. Theory of Finite Deformations of Porous Solids. Indiana University Mathematics Journal 21, 597–620.

Brochard, L., Vandamme, M., Pellenq, R.J.-M., 2012. Poromechanics of microporous media. Journal of the Mechanics and Physics of Solids 60, 606–622.

Brunauer, S., Deming, L.S., Deming, W.E., Teller, E., 1940. On a Theory of the van der Waals Adsorption of Gases. Journal of the American Chemical Society 62, 1723–1732.

Brunauer, S., Emmett, P.H., Teller, E., 1938. Adsorption of Gases in Multimolecular Layers. Journal of the American Chemical Society 60, 309–319.

Campagnolo, J., Akgerman, A., 1995. Modeling of soil vapor extraction (SVE) systems—Part I. Waste Management 15, 379-389.

Chikatamarla, L., Cui, X., Bustin, R.M., 2004. Implications of volumetric swelling/shrinkage of coal in sequestration of acid gases, Coalbed Methane Symposium, Tuscaloosa, AL.

Colina, H., Roux, S., 2000. Experimental model of cracking induced by drying shrinkage. The European Physical Journal E 1, 189-194.

Coussy, O., 2004. Poromechanics. John Wiley & Sons, Ltd, Chichester.

Coussy, O., 2010. Mechanics and physics of porous solids. John Wiley & Sons.

Dąbrowski, A., 2001. Adsorption—from theory to practice. Advances in colloid and interface science 93, 135-224.

de Feijter, J., 1988. Thin Liquid Films.: 1. Thermodynamics of thin liquid films, in: Ivanov, I. (Ed.). CRC Press.

DeHoff, R., 2006. Thermodynamics in materials science. CRC Press.

Derjaguin, B., Kusakov, M., 1936. Contact-line dynamics of a diffuse fluid interface. Izv Akad Nauk SSSR Ser Khim 5, 741.

Dolino, G., Bellet, D., Faivre, C., 1996. Adsorption strains in porous silicon. Physical Review B 54, 17919.

Espinoza, D., Vandamme, M., Dangla, P., Pereira, J.M., Vidal‐Gilbert, S., 2013. A transverse isotropic model for microporous solids: Application to coal matrix adsorption and swelling. Journal of Geophysical Research: Solid Earth 118, 6113-6123.

Everett, D., 1972. Manual of symbols and terminology for physicochemical quantities and units, appendix II: Definitions, terminology and symbols in colloid and surface chemistry. Pure and Applied Chemistry 31, 577-638.

Gor, G.Y., Bernstein, N., 2016. Revisiting Bangham's law of adsorption-induced deformation: changes of surface energy and surface stress. Physical chemistry chemical physics : PCCP 18, 9788–9798.

Gor, G.Y., Huber, P., Bernstein, N., 2017. Adsorption-induced deformation of nanoporous materials—A review. Applied Physics Reviews 4, 011303.

Haines, R.S., McIntosh, R., 1947. Length Changes of Activated Carbon Rods Caused by Adsorption of Vapors. Journal of the American Chemical Society 15, 28–38.

Hansen, W., 1987. Drying shrinkage mechanisms in Portland cement paste. Journal of the American Ceramic society 70, 323-328.

Hol, S., Spiers, C.J., 2012. Competition between adsorption-induced swelling and elastic compression of coal at CO 2 pressures up to 100MPa. Journal of the Mechanics and Physics of Solids 60, 1862-1882.

Israelachvili, J.N., 2011. Intermolecular and surface forces. Academic press.

Kowalczyk, P., Ciach, A., Neimark, A.V., 2008. Adsorption-induced deformation of microporous carbons: pore size distribution effect. Langmuir : the ACS journal of surfaces and colloids 24, 6603–6608.

Lakhanpal, M.L., Flood, E.A., 1957. Stresses and strains in adsorbate–adsorbent systems: Iv. Contractions of activated carbon on adsorption of gases and vapors at low initial pressures. Canadian Journal of Chemistry 35, 887–899.

Langmuir, I., 1918. The adsorption of gases on plane surfaces of glass, mica and platinum. Journal of the American Chemical Society 40, 1361–1403.

Lemmon, E.W., McLinden, M.O., Friend, D.G., NIST chemistry webbook, thermophysical properties of fluid systems, NIST standard reference database number 69. National Institute of Standards and Technology Gaithersburg, MD.

Levine, J.R., 1996. Model study of the influence of matrix shrinkage on absolute permeability of coal bed reservoirs. Geological Society, London, Special Publications 109, 197-212.

Müller, U., Reichert, H., Robens, E., Unger, K., Grillet, Y., Rouquerol, F., Rouquerol, J., Pan, D., Mersmann, A., 1989. High-resolution sorption studies of argon and nitrogen on large crystals of microporous zeolite ZSM-5. Fresenius' Zeitschrift für analytische Chemie 333, 433-436.

Nguyen, H.T., Rahimi-Aghdam, S., Bažant, Z.P., 2019. Sorption isotherm restricted by multilayer hindered adsorption and its relation to nanopore size distribution. Journal of the Mechanics and Physics of Solids 127, 111–124.

Palmer, I., Mansoori, J., 1996. How permeability depends on stress and pore pressure in coalbeds: a new model, SPE Annual Technical Conference and Exhibition. Society of Petroleum Engineers.

Pijaudier-Cabot, G., Vermorel, R., Miqueu, C., Mendiboure, B., 2011. Revisiting poromechanics in the context of microporous materials. Comptes Rendus Mécanique 339, 770-778.

Ravikovitch, P.I., Neimark, A.V., 2006. Density functional theory model of adsorption deformation. Langmuir 22, 10864-10868.

Rusanov, A.I., 1966. Thermodynamics of films. 2. Equilibrium conditions and elasticity of flat thin films. COLLOID JOURNAL-USSR 28, 583–588.

Sarman, S., Eriksson, J.C., Kjellander, R., Ljunggren, S., 1987. Properties of a mean field fluid confined to a narrow slit, Surface Forces and Surfactant Systems. Steinkopff, Darmstadt, pp. 76–86.

Serre, C., Millange, F., Thouvenot, C., Nogues, M., Marsolier, G., Louër, D., Férey, G., 2002. Very Large Breathing Effect in the First Nanoporous Chromium (III)-Based Solids: MIL-53 or $Cr^{III}(OH)\cdot\{O_2C-C_6H_4-CO_2\}\cdot\{HO_2C-C_6H_4-CO_2H\}_x\cdot H_2O_y$. Journal of the American chemical society 124, 13519-13526.

Shuttleworth, R., 1950. The Surface Tension of Solids. Proceedings of the Physical Society. Section A 63, 444–457.

Van Opdenbosch, D., Fritz‐Popovski, G., Wagermaier, W., Paris, O., Zollfrank, C., 2016. Moisture‐Driven Ceramic Bilayer Actuators from a Biotemplating Approach. Advanced Materials 28, 5235-5240.

Vandamme, M., 2019. Coupling between adsorption and mechanics (and vice versa). Current Opinion in Chemical Engineering 24, 12-18.

Vandamme, M., Brochard, L., Lecampion, B., Coussy, O., 2010. Adsorption and strain: The CO2-induced swelling of coal. Journal of the Mechanics and Physics of Solids 58, 1489–1505.

Vermorel, R., Pijaudier-Cabot, G., 2014. Enhanced continuum poromechanics to account for adsorption induced swelling of saturated isotropic microporous materials. European Journal of Mechanics - A/Solids 44, 148–156.

Wien, W., Harms, F., Lenz, H., Bakker, G., 1928. Kapillarität und oberflächenspannung. Akademische Verlagsgesellachaft.

Yakovlev, V.Y., Fomkin, A., Tvardovski, A., 2004. Adsorption and deformation phenomena at interaction of N2 and microporous carbon adsorbent. Journal of colloid and interface science 280, 305-308.

Zhang, Y., 2018. Mechanics of adsorption–deformation coupling in porous media. Journal of the Mechanics and Physics of Solids 114, 31–54.

Zhao, Q., Dunlop, J.W., Qiu, X., Huang, F., Zhang, Z., Heyda, J., Dzubiella, J., Antonietti, M., Yuan, J., 2014. An instant multi-responsive porous polymer actuator driven by solvent molecule sorption. Nature communications 5, 4293.

APPENDIX A. NUMERICAL INTEGRATION SCHEME FOR CALCULATING SURFACE FORCE TERMS

Substituting Eq. (39) and $x = p / p_0$ into Eqs. (36) and (37), we have the dimensionless surface force terms:

$$\Delta\tilde{\Pi}(x,n) = \frac{1}{\Gamma_0}\int_0^x \frac{1}{x}\frac{\partial\Gamma(x,n)}{\partial n}dx \tag{A.1}$$

$$\Delta\tilde{\gamma}_p(x,n) = -\int_0^x \frac{1}{x}\frac{\Gamma(x,n)}{\Gamma_0}dx + \Delta\tilde{\Pi}(x,n)n \tag{A.2}$$

The lower Reimann scheme for numerical integration of the integrands of $\Delta\tilde{\Pi}$ and $\Delta\tilde{\gamma}_p$ requires a discrete set of the integral variable (n_i and x_j), the value of the integrand at those discrete variable points, and a known reference value for the integral ($\Delta\tilde{\Pi}$ and $\Delta\tilde{\gamma}_p$). The reference values are $\Delta\tilde{\Pi}\big|_{x=0,n=\infty} = 0$ and $\Delta\tilde{\gamma}_p\big|_{x=0,n=\infty} = 0$ for large pore in vacuum. Due to the rapid changes of the integrands at lower values of x and n, a logarithmic discretization is used to have more resolution in those regimes. The discretization increments are denoted by $\Delta n_i = n_{i+1} - n_i$ and $\Delta x_i = x_{i+1} - x_i$. The integrand $\partial\Gamma / \partial h / x$, for $\Delta\tilde{\Pi}$, is readily available at any point (n,x) from Eq. (40), thus providing $\Delta\tilde{\Pi}$ at a desired point (n,x). The integrand $\Gamma / \Gamma_0 / x$ of the first integral in Eq. (A.2) is also available through Eq. (38), which combined with $\Delta\tilde{\Pi}$, can give $\Delta\tilde{\gamma}_p$ at any points (n,x). Therefore, Eqs. (A.1) and (A.2) can be integrated by the lower Riemann scheme as:

$$\Delta\tilde{\Pi}(x_l,n_k) = \sum_{i=1}^{l}\Delta x_i \frac{1}{x_i}\frac{1}{\Gamma_0}\frac{\partial\Gamma}{\partial n}(x_i,n_k)\ ;\ \forall k,l \tag{A.3}$$

$$\Delta\tilde{\gamma}_p(x_l,n_k) = -\sum_{i=1}^{l}\frac{1}{x_i}\frac{\Gamma(x_i,n_k)}{\Gamma_0}\Delta x_i + \Delta\tilde{\Pi}(x_l,n_k)n_k\ ;\ \forall k,l \tag{A.4}$$

To enhance the computational efficiency, a grid is created on the $n-x$ plane which has n_i varying in the horizontal direction and x_i in the vertical direction. The summation terms in Eqs. (A.3) and (A.4) can be thus expressed in matrix form for implementation purposes:

$$\left[\Delta\tilde{\Pi}\Big|_{x_l}^{n_1} \quad \cdots \quad \Delta\tilde{\Pi}\Big|_{x_l}^{n_k}\right] = \left[\Delta x_1 \quad \cdots \quad \Delta x_l\right] \times \begin{bmatrix} \frac{1}{x}\frac{\partial\left(\Gamma/\Gamma_0\right)}{\partial n}\Big|_{x=10^{-7}}^{n_1} & \cdots & \frac{1}{x}\frac{\partial\left(\Gamma/\Gamma_0\right)}{\partial n}\Big|_{x=10^{-7}}^{n_k} \\ \vdots & \ddots & \vdots \\ \frac{1}{x}\frac{\partial\left(\Gamma/\Gamma_0\right)}{\partial n}\Big|_{x=x_l}^{n_1} & \cdots & \frac{1}{x}\frac{\partial\left(\Gamma/\Gamma_0\right)}{\partial n}\Big|_{x=x_l}^{n_k} \end{bmatrix} ; \forall l \qquad \text{(A.5)}$$

$$\left[\sum_{i=1}^{l}\frac{1}{x_i}\frac{\Gamma\left(n_k,x_i\right)}{\Gamma_0}\Delta x_i\right] = -\left[\Delta x_1 \quad \cdots \quad \Delta x_l\right] \times \begin{bmatrix} \frac{1}{x}\frac{\Gamma}{\Gamma_0}\Big|_{x=10^{-7}}^{n_1} & \cdots & \frac{1}{x}\frac{\Gamma}{\Gamma_0}\Big|_{x=10^{-7}}^{n_k} \\ \vdots & \ddots & \vdots \\ \frac{1}{x}\frac{\Gamma}{\Gamma_0}\Big|_{x=x_l}^{n_1} & \cdots & \frac{1}{x}\frac{\Gamma}{\Gamma_0}\Big|_{x=x_l}^{n_k} \end{bmatrix} ; \forall l \qquad \text{(A.6)}$$

APPENDIX B. CHOICE OF R_0 AND α

The representative pore size is selected to give approximately the realistic total pore surface area and volume-specific surface area, A_s under given total porosity of the matrix. Let us approximate the pore size distribution in Fig. 8 with a microporous network of spheres with radius $R_{1,0}$ and a mesoporous network of spheres with radius $R_{2,0}$, each constituting r_1 and r_2 fraction of current the pore volume with $r_1 + r_2 = 1$. Based on Eq. (59), the total pore surface areas of the micro- and the meso- pores are respectively given by

$$\mathbb{A}_1 = A_{s,1}\Omega_0 = \frac{3}{R_{1,0}}\left(r_{1,0}\phi_0\right)^{1/3}\left(r_1\phi\right)^{2/3}\Omega_0 \qquad \text{(B.1)}$$

$$\mathbb{A}_2 = A_{s,2}\Omega_0 = \frac{3}{R_{2,0}}\left(r_{2,0}\phi_0\right)^{1/3}\left(r_2\phi\right)^{2/3}\Omega_0 \qquad \text{(B.2)}$$

where $A_{s,k}$ is the specific surface area of each pore family. Summation of Eqs. (B.1) and (B.2) gives the total pore surface area. Assuming that the volume fractions remain unchanged during deformation ($r_1 = r_{1,0}$ and $r_2 = r_{2,0}$) and setting the sum of Eqs. (B.1) and (B.2) equal to the total surface area of a single pore network of spheres with radius R_0, we have

$$R_0 = \left[\frac{r_1}{R_{1,0}} + \frac{r_2}{R_{2,0}} \right]^{-1} \tag{B.3}$$

From Fig. 8, one can read $R_{1,0} = (0.35 + 0.8)/4 = 0.2875\text{nm}$ and $R_{2,0} = 18/2 = 9\text{nm}$. The total pore volume per grams of sample is $0.86\text{cm}^3/\text{g}$ while the microporous network volume per grams of sample is $0.20\text{cm}^3/\text{g}$. Thus, we have $r_1 = 0.20/0.86 = 0.23$ and $r_2 = 1 - r_1 = 0.77$, giving $R_0 = \left[0.23/0.2875 + 0.77/9\right]^{-1} = 1.13\text{nm}$.

The parameter α is defined to map the adsorptive behaviour of a sphere pore of radius R_0 to that of a slit pore of width $h = \alpha R_0$. A natural assumption is to define α such that the slit pore has the same volume as the sphere pore to preserve the total porosity of the REV. The volume of the slit pore is given by

$$V_{slit} = A_{slit} h \tag{B.4}$$

where A_{slit} is the area of each surface in the slit-pore. Equating the surface area of the slit pore and the spherical pore, $A_{slit} = A_{sphere}/2$, and setting $V_{slit} = V_{sphere}$ gives:

$$h = \frac{2V_{sphere}}{A_{sphere}} = \frac{2}{3} R_0 \tag{B.5}$$

Thus $\alpha = 2/3$.

APPENDIX C. DUAL-PORE MODEL FORMULATION

Consider a pore network consisting of two families of pores with radii $R_{1,0}$ and $R_{2,0}$. The volume fraction of each family r_k is defined with respect to the total void volume:

$$\Omega_k^v = r_k \Omega^v = r_k \phi \Omega_0 = \phi_k \Omega_0 \tag{C.1}$$

where $k = 1, 2$; ϕ_k is the porosity contribution of each pore family. Obviously, $r_1 + r_2 = 1$ and $\phi_1 + \phi_2 = \phi$. Using Eq. (59), one can write the surface area of each pore network as

$$\mathbb{A}_k = \frac{3}{R_{k,0}} \phi_{k,0}^{1/3} \phi_k^{2/3} \Omega_0 \tag{C.2}$$

Substituting Eq. (C.1) into (C.2) gives the total pore surface area:

$$\mathcal{A} = \mathcal{A}_1 + \mathcal{A}_2 = \left[\frac{3}{R_{1,0}} r_{1,0}^{1/3} r_1^{1/3} + \frac{3}{R_{2,0}} r_{2,0}^{1/3} r_2^{1/3} \right] \phi_0^{1/3} \phi^{2/3} \Omega_0 \tag{C.3}$$

and by definition of A_s, we have:

$$A_s = 3\phi_0^{1/3} \phi^{2/3} \left[\frac{1}{R_{1,0}} r_{1,0}^{1/3} r_1^{1/3} + \frac{1}{R_{2,0}} r_{2,0}^{1/3} r_2^{1/3} \right] \tag{C.4}$$

Assuming that the volume fractions remain unchanged during deformation ($r_k = r_{k,0}$), Eq. (C.4) simplifies to

$$A_s = 3\phi_0^{1/3} \phi^{2/3} \left[\frac{r_1}{R_{1,0}} + \frac{r_2}{R_{2,0}} \right] \tag{C.5}$$

The smearing of adsorption stresses shall be sought by revisiting the thermodynamics involving the pore fluid and the interface. One can rewrite Eq. (24) for single-species adsorbate interacting with the pores in family k as:

$$dF_k^{surf} = -S_k^{surf} dT - \Pi_k d\Omega_k^v + \gamma_{p,k} d\mathcal{A}_k + \mu dN_k^{surf} \tag{C.6}$$

where Π_k and $\gamma_{p,k}$ are given by Eqs. (36) and (37). Summation of Eq. (C.6) over the two pore families gives the Helmholtz free energy of the total pore surface:

$$dF^{surf} = -S^{surf} dT - \overbrace{\left(\Pi_1 \frac{\partial \Omega_1^v}{\partial \Omega^v} + \Pi_2 \frac{\partial \Omega_2^v}{\partial \Omega^v} \right)}^{\bar{\Pi}} d\Omega^v + \overbrace{\left(\gamma_{p,1} \frac{\partial \mathcal{A}_1}{\partial \mathcal{A}} + \gamma_{p,2} \frac{\partial \mathcal{A}_2}{\partial \mathcal{A}} \right)}^{\bar{\gamma}_p} d\mathcal{A} + \mu dN^{surf} \tag{C.7}$$

Comparison of Eqs. (24) and (C.7) reveals the smearing relations for Π and γ_p at continuum scale:

$$\bar{\Pi} = \Pi_1 \frac{\partial \Omega_1^v}{\partial \Omega^v} + \Pi_2 \frac{\partial \Omega_2^v}{\partial \Omega^v} \text{ and } \bar{\gamma}_p = \gamma_{p,1} \frac{\partial \mathcal{A}_1}{\partial \mathcal{A}} + \gamma_{p,2} \frac{\partial \mathcal{A}_2}{\partial \mathcal{A}} \tag{C.8}$$

Considering $\partial\Omega_k^v / \partial\Omega^v = r_k$ and substituting Eqs. (C.1) and (C.2), one can write

$$\frac{\partial \mathcal{A}_k}{\partial \mathcal{A}} = \frac{r_k / R_{k,0}}{r_1 / R_{1,0} + r_2 / R_{2,0}} \tag{C.9}$$

Eqs. (C.5), (C.8) and (C.9) complete the dual-pore model and can be readily substitute into Eqs. (55) and (57) for REV simulations.